Interpretable single-cell factor decomposition using sciRED

Delaram Pouyabahar (1,2), Tallulah Andrews (7,8), Gary D. Bader (1,2,3,4,5,6,9)

1 - Department of Molecular Genetics, University of Toronto, Toronto, Ontario, Canada
2 - The Donnelly Centre, University of Toronto, Toronto, Ontario, Canada
3 - Department of Computer Science, University of Toronto, Toronto, Ontario, Canada
4 - Lunenfeld-Tanenbaum Research Institute, Toronto, Ontario, Canada
5 - Princess Margaret Research Institute, University Health Network, Toronto, Ontario, Canada
6 - CIFAR Multiscale Human Program, CIFAR, Toronto, Ontario, Canada
7 - Department of Biochemistry, Schulich School of Medicine and Dentistry, University of Western Ontario, London, Ontario, Canada
8 - Department of Computer Science, University of Western Ontario, London, Ontario, Canada
9 - Corresponding author

Abstract

Single-cell RNA sequencing (scRNA-seq) maps gene expression heterogeneity within a tissue. However, identifying biological signals in this data is challenging due to confounding technical factors, sparsity, and high dimensionality. Data factorization methods address this by separating and identifying signals in the data, such as gene expression programs, but the resulting factors must be manually interpreted. We developed Single-Cell Interpretable Residual Decomposition (sciRED) to improve the interpretation of scRNA-seq factor analysis. sciRED removes known confounding effects, uses rotations to improve factor interpretability, maps factors to known covariates, identifies unexplained factors that may capture hidden biological phenomena and determines the genes and biological processes represented by the resulting factors. We apply sciRED to multiple scRNA-seq datasets and identify sex-specific variation in a kidney map, discern strong and weak immune stimulation signals in a PBMC dataset, reduce ambient RNA contamination in a rat liver atlas to help identify strain variation, and reveal rare cell type signatures and anatomical zonation gene programs in a healthy human liver map. These demonstrate that sciRED is useful in characterizing diverse biological signals within scRNA-seq data.

Introduction

Single-cell RNA sequencing (scRNA-seq) maps heterogeneity in gene expression in large cell populations. This heterogeneity can be attributed to various factors, both observed and hidden[1]. We can broadly categorize sources of this heterogeneity into sample-level factors, such as experimental conditions or age and weight of patients, cell-level covariates like cell type identity, cell cycle stage, and library size, or as gene-level attributes such as pathways. Each of these categories can be further classified based on their biological or technical nature and whether they are known during experimental design, or observed in or inferred based on the data. Despite their importance, identifying and interpreting factors in scRNA-seq data remains challenging due its noise, sparsity, and high dimensionality[2].

Matrix factorization (or decomposition) can identify multiple factors (signals) in a cell by gene scRNA-seq data matrix, each one capturing a unique pattern of covarying gene expression values that may represent a covariate, such as a set of genes affected by batch or a biological gene expression program[3]. Many factorization methods exist[4,5,6,7,8,9,10,11,12,13], however they generally only identify factors and leave interpretation up to the user. Some recent methods, such as scLVM[14], fscLVM[15] and

1

Spectra[16], can automatically interpret factors by matching them to pre-annotated gene sets (e.g. pathways), but do not consider a wider range of covariates important in single cell genomics data, such as sample-level attributes. To address this challenge, we developed Single-Cell Interpretable Residual Decomposition (sciRED) to aid in scRNAseq factor analysis and interpretation.

sciRED enables factor discovery and interpretation in the context of known covariates and biological gene expression programs. sciRED provides an intuitive visualization of the associations between factors and covariates, along with a set of interpretability metrics for all factors. These metrics identify clear factor-covariate pairs as well as factors not matching known covariates but which are potentially interpretable. Factor correlated genes and pathways also aid in interpretation. We apply sciRED to diverse datasets including the scMixology benchmark and four biological single-cell atlases that contain known factors. We showcase its application in identifying cell identity programs and sex-specific variation in a kidney map, discerning strong and weak immune stimulation signals in a PBMC dataset, reducing ambient RNA contamination in a rat liver atlas to unveil strain-related variation, and revealing hidden biology represented by rare cell type signatures and anatomical zonation gene programs in a healthy human liver map. These demonstrate the utility of sciRED for characterizing diverse biological signals within scRNA-seq datasets.

Results

sciRED implements a four-step factor characterization approach for an input cell by gene matrix: (1) Remove known confounding effects, factorize the residual matrix to identify additional factors not accounted for by confounding effects, and use rotations to maximize factor interpretability; (2) Automatically match factors with covariates of interest; (3) evaluate unexplained factors that may indicate hidden biological phenomena; (4) Determine the genes and biological processes represented by factors of interest (Figure 1A). In the factor discovery phase, sciRED removes user-defined unwanted technical factors, such as library size and sample or protocol, as covariates within a Poisson generalized linear model (GLM)[17]. This regresses out the covariates and produces Pearson residuals. These residuals are then factored using PCA with varimax rotation[18] to enhance interpretability (Figure 1B). To identify factors that explain a specific covariate, sciRED attempts to find matching labels (e.g. cell types, covariates of interest) for each factor using an ensemble classifier (see methods). Each cell is represented as a vector of factor weights, which are classified to predict covariate labels (e.g. "female" or "male" factors in the covariate "biological sex") using four machine learning classifiers (logistic regression[19], linear classifier/area under the curve (AUC)[20,21], decision tree[22], and extreme gradient boosting (XGB)[23]). Each factor is a feature and feature selection across an ensemble of these classifiers generates factor-covariate-level association (FCA) scores, which are visualized as a heat map. To identify high-scoring factor-covariate pairs, we use three approaches. First, we use visual inspection of the FCA heatmap. Second, we compare the association scores of each factor to the background distribution of values in the FCA table to automatically highlight significant associations (see Methods, Figure 1C). Third, we calculate a specificity measure to determine whether an explained factor captures the gene expression program related to a unique covariate or is associated with multiple covariate levels simultaneously. Interpretation is often easier when a factor matches only one covariate level.

The third step of sciRED evaluates unexplained factors for potential interpretability using three types of metrics: separability, effect size, and homogeneity which are presented as a factor-interpretability

score (FIS) table (Figures 1D, S1, see Methods). For unexplained factors that should be prioritized for follow up exploration because they may contain a hidden signal, ideally cells should be scored highly by the factor (measured by effect size), there should be two populations of cells, ones that score highly and ones that don't (bimodal distribution measured by separability) and the potential new signal is expected to be strong in cells ranked highly by that factor and other signals (e.g. known technical covariates) should be evenly distributed across this ranking (measured by homogeneity). The fourth step evaluates the factor loadings (gene lists) for biological signals. This involves manually investigating top genes and enriched pathways associated with the factor (Figure 1E).

sciRED improves factor discovery

To demonstrate the enhanced interpretability of factors achieved by first regressing out technical confounders, we analyzed the SCMixology[24] benchmarking dataset using sciRED and compared it to a standard PCA analysis applied directly to the cell by gene matrix (Figures S2, See methods). This dataset comprises scRNAseq profiles from a mixture of three cancer cell lines (H2228, H1975, HCC827), sequenced in three batches using different library preparation platforms (Dropseq, Celseq2, 10X). Comparing the sciRED FCA table to PCA on log-transformed data demonstrates that sciRED improves one-to-one matching between factors and covariates, which is also visually evident in factor scatterplots (Figure S2A-D). For example, PCA1 shows a correlation with library size and PC5 captures both the cell identity of H1975 cell lines and HCC827 cellular programs (Figure S2A, S2C, and S2EF). On the other hand, sciRED factors F1 and F4 capture each HCC827 and H1975 cell line gene expression programs independently and do not have any factors correlated with library size. This example shows that sciRED identified factors can be more easily interpretable than those identified using PCA.

sciRED finds cell type identity programs and sex-specific processes in a human healthy kidney map

We applied sciRED to a single-cell map of healthy human kidneys (Figure 2) obtained from 19 living donors, with nearly equal contributions from both females and males (10 female, 9 male)[25]. sciRED successfully identified cell type identity programs for diverse kidney cell types (Figure 2AB, Figure S3, Table S1) as well as a factor representing sex-specific differences. For instance, factors F1 and F13 capture the identity programs of proximal tubules and endothelial cells, respectively, while F18 represents sex-specific differences (Figure 2C). Factor F18 has a high association score with male and female covariates based on the FCA heatmap, indicating it has captured sex variation. Further evaluation of the distribution of factor F18 across different cell types reveals a cell-type dependent distribution of sex-related variation, with a strong representation in the proximal tubule cell type population (Figure 2D). The FIS heatmap indicates that F18 is highly specific and shows a low homogeneity score across sex covariates, confirming that cells from male and female individuals are not uniformly distributed along F18 (Figure 2E). Consistent with the original study, pathway analysis shows an increase in processes related to aerobic metabolism (such as aerobic respiration, oxidative phosphorylation, tricarboxylic acid (TCA) cycle, and electron transport chain) in males (Figure 2FG). These findings align with the higher basal respiration and ATP-linked respiration processes in males, as functionally validated in the original study[25]. This highlights sciRED's ability to identify cell type identity signatures and sample covariate-specific variation.

sciRED identifies stimulation signals across lymphoid and myeloid cells in a stimulated PBMC dataset

We used sciRED to analyze a benchmark dataset comprising 10x droplet-based scRNA-seq PBMC data from eight lupus patients before and after a 6-hour treatment with interferon (IFN)-β[26] (Figure 3). Our sciRED analysis successfully identifies cell type identity programs and stimulation-to-control axes of variation (Figure 3A, Table S1). We identified two factors, F9 and F2, which capture stimulation signals (Figure 3B). The FIS table indicates a high bimodality (separability) score for both factors, a high effect size for F2, and high specificity for F9 (Figure 3C), illustrating the utility of the FIS table for capturing biological signals. Differential evaluation of the cell type representation within the two factors reveals a predominance of lymphoid and myeloid cells for F9 and F2, respectively (Figure 3D). In particular, F9 represents a stronger overall stimulation signal and stimulation in lymphoid populations and F2 captures a stimulation signal in myeloid populations. Examination of the cell type distribution across F9 and F2 highlights distinct clustering between the non-stimulated control and stimulated groups along both factors (Figure 3EH). Immune response-related genes and biological processes, including interferon signaling, stress or pathogen response, and cytokine signaling, are enriched in both factors (Figures 3F,G,I,J). This indicates sciRED's ability to identify both cell-type-specific gene expression activity programs, including stimulated cellular states.

sciRED alleviates ambient RNA contamination for group-based comparison

We applied sciRED to a healthy rat liver atlas mapped in Dark Agouti (DA) and Lewis (LEW) strains[27]. This atlas contains hepatocyte-derived ambient RNA contamination, a known artifact likely caused by fragile hepatocytes leaking RNA into the cell homogenate before sequencing[28]. sciRED identified factors with cell type identities, as expected, along with two factors capturing strain-associated variation (F6 and F20) (Figure 4A-F, Table S1). The FIS table shows that factor F6 has high specificity and separability, as well as low strain homogeneity (Figure 4B). Factor F20 is the second strongest factor following F6 (Figure 4BC). F6 and F20 represent strain differences within the hepatocyte (Figure 4D) and myeloid cell types (Figure 4EF, Figure S4), respectively. Standard differential expression analysis is not able to identify this signal due to strong ambient RNA contamination[27] (Figure 4G). For instance, four hepatocyte genes—*Fabp1*, *Tmsb4x*, *Fth1*, *Apoc1*—are among the top differentially expressed genes within the myeloid cell type of both DA and LEW strains and are estimated to be ambient RNA by SoupX[29] (Figure 4G, Table S2, see Methods). However, the top 50 myeloid strain-associated genes identified by sciRED F20 are free of such contaminants (Figure 4H, Table S1). These myeloid specific strain variations were experimentally validated in the original study. This shows the utility of sciRED in deconvolving biological signals from contamination to facilitate factor interpretation and group-based comparisons.

Exploring hidden biology in the healthy human liver atlas captured by unannotated factors

We applied sciRED to a healthy human liver atlas[30] and explored the unannotated biological signals (Figure S5, Table S1). sciRED's FCA heatmap shows that most signals correspond to liver cell type identity programs (Figure 5A). For example, F3 most strongly captures the cell identity of liver sinusoidal endothelial cells (LSECs), while F4 captures non-inflammatory macrophages. The FCA heatmap highlights nine factors (1, 10, 19, 20, 22, 26, 28, 29, 30) that are not associated with annotated cell types (Figure 5B). To discern whether these factors represent technical or biological signals, we calculated the correlation between each factor and three major technical covariates—library size, number of expressed genes, and percentage of mitochondrial gene

4

expression—as well as cell cycle (S and G2M) phase scores (Figure 5C). Out of the nine factors, F1, F20, F22, F29 are correlated with technical and cell cycle covariates (R>0.45), leaving five (F10, F19, F26, F28, F30) that may represent unannotated biological signals. Evaluating the FIS table reveals that, among the five factors analyzed, all except F19 are well-mixed based on the sample covariate, suggesting a possible sample-specific effect for F19. F10 stands out with a higher bimodality score, indicating it more effectively separates a subpopulation of cells. These factors exhibit a low effect size, indicating weak signals (Figure 5D). Factor F10 exhibits significant enrichment of a subpopulation of cells within the cholangiocyte cluster (Figure 5E). The top loaded genes within this factor include *MUC5A*, *MUC1*, *TFF1*, *LGALS2*, *SLPI*, *TFF2*, *TFF3*, *KRT19*, *LGALS4*, and *PIGR*. The enrichment of biological processes such as ion export, regulation of transport activity, localization, and response to ER stress strongly suggests that F10 has captured the cellular program of a rare population of mucus-producing cholangiocytes that was not identified in the original study but was reported in a more comprehensive subsequent human liver single cell map[31]. Factor F30, is enriched within a subpopulation of cells labeled as plasma cells in the original map (Figure 5F). The top genes in the loading vector include IgK+IgG+ B cell marker genes, including *IGHG4*, *IGHG1*, *IGHG3*, *IGKV1-12*, *HERPUD1*, *IGKV1-18*, *IGKC*, *SSR4*, *IGKV3-20*, and *IGKV3-21* (Figure 5F). Pathway enrichment analysis highlights biological processes such as protein folding and maturation, antibody-mediated complement activation, protein transport, and ER to cytosol transport (Figure 5F). These findings suggest that F30 may represent an antibody-secreting IgK+IgG+ B cell[31] gene expression program, not described in the original study due to its low frequency, but later captured in an expanded human liver single-cell map[31]. Factor F19 is enriched in two hepatocyte clusters, Hep1 and Hep2, which were annotated as pericentrally zoned hepatocytes in the original study (Figure 5G). The presence of pericentral markers such as *CYP3A4*, *GLUL*, and *OAT*, along with enrichment in biological processes such as xenobiotic metabolic processes, small molecule metabolism, and lipid and fatty acid metabolism, suggests that F19 captures the anatomical pericentral signature within the hepatic lobules[28,30,32](Figure 5G). Factor F28, is correlated with cell cycle signatures and inversely enriched within a population of gd T cells (Figure 5H). The top loaded genes for F28 include cell-cycle-related regulatory genes *UBE2C*[33], *TOP2A*[34], *KPNA2*[35], *CKS2*[36], and *BIRC5*[37] and pathway analysis reveals enrichment in cell cycle and cell division, RNA splicing and processing, and nuclear division (Figure 5H). Together, these results suggest that this factor captures the cell cycle state within the gd T cell subset. We could not clearly interpret factor F26. In conclusion, sciRED is able to identify weak signals, such as rare cell types and subtle cell states, that were overlooked by standard single-cell analysis pipelines in the original study.

Discussion

We developed sciRED, a novel single cell transcriptomics data interpretation method that combines unsupervised factor analysis and supervised covariate modeling to identify biological and technical signals within single cell transcriptomics data. We introduce new metrics to assess factor interpretability to help characterize known and unknown sources of variation in the data. We also showed that regressing out known technical factors before factorization aids in data interpretation.

To test sciRED, we analyzed a series of datasets with diverse known covariates and showed that sciRED could recover these. This works well, but may miss uninterpreted signals in the original data. Although many single-cell transcriptomics simulation tools exist[9,38–43] to assist in benchmarking analysis methods, there has been little focus on factor simulation. We simulated factors to evaluate

interpretability metrics, but our approach was simplistic and can be improved. sciRED uses PCA coupled with varimax rotation as a high performing matrix decomposition method, though many other factor analysis methods exist[44] and could be evaluated to see if they can improve performance. Tools dedicated to simulating loading and score matrices from single-cell transcriptomics, ranging from simple to complex structures, could aid in benchmarking the performance of matrix factorization methods across different scenarios. Such tools could also help answer questions such as determining the minimal sample size required to recover a factor with weak loadings. These simulation methods could draw inspiration from factor simulation techniques used in psychometric studies[45–48].

We present a suite of metrics designed to evaluate the interpretability of factors derived from a matrix factorization method within a single dataset. These metrics help identify which of the K factors generated by a given factorization algorithm are likely to be interpretable. However, factor distributions can exhibit various patterns that the provided metrics may not fully capture. For unexplained factors, even one high metric value can be sufficient to highlight them as potentially interesting. In such cases, further interpretation should rely on enriched genes and pathways. Moreover, the optimal factorization method and its specific settings—such as the number of genes included—may vary depending on the input dataset. Variables like sample complexity (including diversity of cell types, presence of rare populations, and number of covariates in the experimental design), signal-to-noise ratio (including contamination level and dropout rate), number of batches, and variation in dissociation protocols and capture technologies in multi-sample studies can influence the choice of factorization method. Developing metrics to compare and identify the optimal factor analysis method and its parameter settings to generally improve interpretability across different methods would be beneficial but remains a challenge.

In sciRED we focused on matrix factorization. However, a limitation of this approach is the assumption that cells can be represented as linear combinations of gene expression signatures, which may limit our ability to capture non-linear patterns. Alternative approaches, such as deep learning-based latent variable models like variational autoencoders (VAEs), can incorporate non-linearities and interactions between latent variables[49] in the factorization step. While the interpretability measures we developed would be applicable to VAE-derived latent spaces, non-linear patterns may inherently be more challenging to interpret. Thus, there remains a trade-off between interpretability and the ability to model complex biological phenomena effectively. The proportion of cellular programs that can be effectively captured by linear versus non-linear approaches remains uncertain for any given dataset. Enhancing the interpretability of deep learning-based models, such as VAEs, while maintaining their ability to capture complex biological phenomena is an active research area[50,51].

We only consider applying sciRED to scRNAseq data. However, it could be applied to bulk RNAseq datasets with tens to hundreds of samples. sciRED could also be extended to function with spatial and multi-omics data with multi-sample datasets, appropriate factor analysis methods and a good understanding of how technical variation affects these data. We expect that as single-cell and multi-omics technologies evolve, integrating and comparing factors extracted from many datasets and various data modalities will deepen our understanding of cellular systems in healthy and diseased tissue.

Main Figure Legends

Figure 1) sciRED overview. A) sciRED comprises four main steps: factor discovery, factor interpretation, factor evaluation and biological characterization. B) In the factor discovery step, a Poisson generalized linear model is applied to the data to remove technical covariates, followed by extraction of residuals and factorization using PCA. The resulting score and loading matrices are then rotated for enhanced interpretability. The score matrix represents the projection of the original data onto the new factor space, illustrating the relationship between cells and factors. Each entry in this matrix reflects how much each cell contributes to the factors. The loading matrix contains the weights or coefficients that define the factors as linear combinations of the original genes. These weights can be used to rank genes according to their contribution to each factor, facilitating further interpretation of the factors. C) Factor interpretation uses an ensemble classifier to match factors with given covariates, generating a Factor-Covariate Association (FCA) table. Covariate-matched factors are identified by thresholding FCA scores based on the distribution of all FCA scores. Unannotated factors may capture novel biological processes or other covariates. D) Factor-interpretability scores (FIS) are computed for each factor. E) The top genes and enriched pathways associated with a selected factor are identified for manual interpretation.

Figure 2) Deciphering cell type identity programs and sex-specific processes in a human healthy kidney map. We applied sciRED to a single-cell healthy human kidney map obtained from 19 living donors, with similar contributions from both females and males. A) FCA heatmap with covariate levels as rows and associated factors as columns. Arrow highlights factor F18 which demonstrates a high association score with female and male covariates. B) FCA score distribution for all factors. The red line indicates the automatically defined threshold used to identify significant factor-covariate matches in the heatmap in A. C) FIS heatmap representing the interpretability scores of the selected factors. Distribution of cells over factor F1 and factor F18 colored based on D) sex and E) cell type covariates indicates the predominant representation of sex-related variation within the proximal tubule

cell type. F) Pathway analysis results on the top positive (female) and negative (male) loaded genes of factor F18. G) Top 20 positively and negatively loaded genes of factor F18.

Figure 3) Identifying interferon-β stimulation signals across lymphoid and myeloid cells in a PBMC dataset. We used sciRED to analyze PBMC scRNA-seq from eight lupus patients before and after an interferon-β (IFN-β) treatment. A) FCA heatmap displaying covariate levels as rows and associated factors as columns. Arrows highlight factors F9 and F2, which capture simulation signals. B) FIS heatmap illustrating the interpretability scores of the selected factors. Red boxes highlight factors capturing IFN-β simulation. C) Sorted factors based on FCA score values for the stimulated covariate level. F9 and F2 are the top factors associated with the stimulation covariate. D) Cell distribution over factors F9 and F2, colored based on cell type covariates. The red dashed line represents the diagonal line passing through the origin. Solid lines are the regression lines that fit each cell type. Lines with larger slopes than the diagonal represent cell types with higher association with F9, while lines with smaller slopes represent cell types more associated with F2. E) Distribution of cells over factors F9 and F1 colored based on simulation/control covariates, revealing distinct clustering between control and stimulated groups along the F9 axis. F) Pathway analysis based on the top-loaded genes of factor F9. G) Top 30 positively loaded genes of factor F9. H) Distribution of cells over factors F1 and F2 colored by simulation state covariate ("stimulated" or "control"/non-stimulated). I) Pathway analysis based on the top-loaded genes of factor F2. J) Top 30 positively loaded genes of factor F2.

Figure 4) sciRED identifies strain-based variation despite ambient RNA contamination in a rat liver map. We applied sciRED to a healthy atlas of the rat liver from two rat strains, Dark Agouti (DA) and Lewis (LEW) containing hepatocyte-derived ambient RNA contamination. A) FCA heatmap displaying covariate levels as rows and associated factors as columns. C) Factors F6 and F20 are most associated with strain variation. B) FIS heatmap illustrating the interpretability scores of the selected factors. D) Distribution of cells over factors F6 vs. F1 colored by strain and E) factors F20 vs. F1 colored by strain and F) by cell type, indicating that factor F20 captures strain variation within the myeloid population. G) Volcano plot of differential expression between strains within myeloid cells. Red dots are hepatocyte-derived ambient RNA transcripts as estimated by SoupX. Four hepatocyte genes—*Fabp1*, *Tmsb4x*, *Fth1*, and *Apoc1*—are labeled among the top differentially expressed genes within the myeloid cell type of both DA and LEW strains. These genes are among the top 50 ambient RNA transcripts derived from SoupX in all four rat liver samples (Table S2). H) Top 50 myeloid strain-associated genes identified by sciRED factor 20, free of contamination from hepatocyte-derived ambient RNA.

Figure 5) Exploring hidden biology in the healthy human liver atlas using unannotated factors. We demonstrate how sciRED facilitates the identification of hidden biology in a healthy human liver single-cell transcriptomic atlas. A) sciRED's FCA heatmap reveals signals corresponding to human liver cell type identity gene expression programs. B) Distribution of the number of matched covariate levels per factor identifies nine unannotated factors (F1, F10, F19, F20, F22, F26, F28, F29, F30) not associated with any given covariate. C) Correlation analysis between unannotated factors and technical covariates (library size, number of expressed genes, percentage of mitochondrial gene expression) and cell cycle (S and G2M) phase scores. D) FIS heatmap indicating the interpretability scores of unexplained factors uncorrelated with technical covariates. E-H) The first row shows the

distribution of selected factors on the atlas tSNE plot, where each dot represents a cell, and colors indicate factor score values. The second row presents boxplots of factor scores across cell types. The third row displays the top-loaded genes, and the fourth row provides pathway analysis for factors E) F10, F) F30, G) F19, and H) F29. E) Factor 10 exhibits significant enrichment within a subpopulation of cells within the cholangiocyte cluster, suggesting the capture of a rare population of mucus-producing cholangiocytes. F) Factor 30 demonstrates positive enrichment within a subpopulation of cells labeled as plasma cells in the original map, suggesting that it captures antibody-secreting IgK+IgG+ B cells. G) Factor 19 is positively enriched in pericentrally zoned hepatocytes (clusters Hep1 and Hep2), capturing an anatomical pericentral gene expression signature within hepatic lobules. H) Factor 28 is correlated with cell cycle signatures and inversely enriched within a population of gd T cells, suggesting capture of cell cycle state within this T cell subset.

Supplementary Figure Legends:

Supplementary Figure 1) Schematic overview of factor interpretability metrics. The four categories of factor interpretability metrics: separability, effect size, specificity, and homogeneity. Separability and effect size are label-free metrics, while specificity and homogeneity are label-dependent.

Supplementary Figure 2) Enhanced interpretability of factors achieved by removing technical confounders. To showcase the enhanced interpretability of factors achieved by regression out technical confounders, we applied PCA and sciRED to the SCMixology benchmarking dataset. We compared how each method captured the H2228, H1975, and HCC827 cell identity programs. FCA tables of A) PCA and B) sciRED demonstrate that PCA captures H1975 and HCC827 gene expression programs in a single factor F5, while sciRED separates the identity programs of each of the three cell lines into separate factors (F1, F2, F5). C and D show a scatter plot of PCA and sciRED factors colored based on cell line and protocol. Correlations between E) PCA and F) sciRED factors with library size suggest that PCA's F1 is predominantly influenced by the library size confounder.

Supplementary Figure 3) The complete factor-covariate association table of the healthy kidney atlas. Association scores between all 30 factors and the sex and cell type covariate levels are shown. sciRED provides both the complete table and a filtered table, which includes factors with at least one association score exceeding the threshold defined over the entire distribution.

Supplementary Figure 4) Annotated healthy rat liver map. A) UMAP visualization of annotated healthy rat liver map, each dot represents a cell, with colors indicating cell types. B) Boxplot depicting the distribution of factor F20 across different cell types.

Supplementary Figure 5) Annotated healthy human liver map. t-SNE distribution of annotated healthy human liver map, each dot represents a cell, with colors indicating cell types.

Supplementary Figure 6) Enhancement in identifying cell line-specific factors through rotations. FCA tables depict A) PCA, B) sciRED, and C) Promax-rotated PCA factors obtained from the Pearson residual of the SCMixology dataset after regressing protocol and library size covariates.

D) Correlation heatmap illustrates the relationship between varimax and PCA factors. E) Correlation heatmap between sciRED (varimax-rotated) and promax factors.

Supplementary Figure 7) Performance evaluation and benchmarking of sciRED. A) Permutation tests were used to assess the significance of each covariate-factor association metric (see methods). B) Comparison of AUC, K-Nearest Neighbors (KNN), logistic regression, decision tree, random forest, and XGB using permutation tests on the scMixology benchmark dataset. We expect the unshuffled (baseline) scores to be higher than the shuffled association scores. KNN's poor performance led to its exclusion from the sciRED ensemble model. The importance scores of each model were min-max scaled for comparison. C) Run time evaluation resulted in the exclusion of the random forest method due to inferior scalability performance. D-G) Benchmark analysis illustrates sciRED's superior performance relative to single classifiers. We assessed the average number of significant matched factors per covariate level for the D) human kidney map, E) human liver map, F) scMixology dataset and G) stimulated PBMC dataset at a significance level of p-value=0.05. The dashed line denotes the value of one factor-covariate association. Model distributions closer to a mean of one and lower variance suggest improved specificity and stability. (ns: p > 0.05, *: p <= 0.05, **: p <= 0.01, ***: p <= 0.001, ****: p <= 0.0001)

Supplementary Figure 8) Optimizing ensemble design through permutation-based comparison of scaling and mean calculation methods. We compared three scaling methods (standardization, min-max scaling, and rank-based) and two mean calculation approaches (arithmetic and geometric) to design an optimal ensemble. sciRED uses standardization scaling and arithmetic mean calculation, which is the optimal combination based on analysis in this figure (panels A, B are for results based on the scMixology dataset and panels C, D are for results based on the healthy human liver dataset). We used the average number of significant associated factors per covariate (p-value=0.05) along the Gini coefficient[52] (see methods) for comparing ensemble designs. Ideally, the average number of significant associated factors per covariate would be close to one, and the Gini coefficients of the shuffled datasets are expected to be less than for the unshuffled data. A) Average number of significant associated factors per covariate (p-value=0.05). The dashed line indicates the value of one factor-covariate association, while the grey area represents the approximate acceptable range. Distributions closer to a mean of one indicate improved specificity. B) Distribution of Gini coefficient calculated for FCA tables of shuffled datasets for each ensemble table. Red dots represent the Gini coefficient of the unshuffled dataset's FCA table, expected to be higher than for the shuffled data (see methods). C) Box plot representing the average number of significant associated factors per covariate (p-value=0.05) for the healthy human liver dataset based on various residual types. Deviance, response and Pearson residuals show comparable performance with Pearson showing lower variance for sciRED (standardization, arithmetic mean). D) Boxplots indicating the distribution of the Gini coefficient calculated for FCA tables of shuffled datasets for each ensemble model and residual type. Deviance, response, and Pearson residuals show comparable results. This analysis reveals that sciRED exhibits superior performance compared to geometric-standard, geometric-rank, and arithmetic-rank methods, as evidenced by the Gini measure. Furthermore, it outperforms ensembles utilizing min-max (which tend to exhibit high false negatives) and rank-scaled methods (associated with high false positives) when considering the average number of significant factors per covariate. The ensemble model was constructed by standardizing the importance scores of AUC, logistic, XGB, and decision tree, followed by arithmetic mean calculation.

Supplementary Figure 9) Impact of residual choice on factor interpretability. We investigated how various residual-based normalization methods affect downstream analysis, as explored by several studies[11,53,54]. Specifically, we examined the impact of different residual types (response, Pearson, and deviance) on factor interpretability performance using the healthy human liver atlas. We employed a permutation test to evaluate the significance of each covariate-factor association based on empirical p-value calculation. Using this approach, we calculated the average number of significant associated factors per covariate (p-value =0.05). Our permutation analysis revealed consistent outcomes across all residual types for most models, with the exception of the response residual-based logistic regression model, which exhibited less stable results. This analysis underscores the robustness of sciRED's performance across different residual types. Consequently, we chose the Pearson residual as the default approach, given its widespread adoption in the field. The dashed line indicates the value of one factor-covariate association, and the grey area represents the approximate acceptable range. E) Similar to Figure D, a permutation analysis was performed on the healthy human liver atlas to evaluate the impact of residual types. Investigation of response, Pearson, and deviance residuals led to consistent performance of models considering known covariates in the scMixology dataset, with sciRED outperforming single classifiers.

Supplementary Figure 10) Evaluating factor interpretability metrics through factor simulation. Factors were simulated to evaluate the effectiveness of the proposed factor interpretability metrics.
A) Simulation assumes that factors are generated from a Gaussian mixture distribution, where each Gaussian represents cells associated with a covariate level. Correlation between the overlap of the two Gaussian distributions and the metric value was used to assess interpretability. B) Factors with greater overlap values would exhibit lower separability and specificity scores (negative correlation), along with higher homogeneity values (positive correlation), and vice versa. C) Distribution of correlation scores for each metric across various categories. The ideal correlation value is represented by a dashed red line for each interpretability category.

Supplementary Tables:
Table S1. Factor loading tables for all biological datasets.
Table S2. SoupX ambient RNA contamination estimates for each rat liver sample.

Methods

sciRED factor discovery framework

We model the read counts for n cells and g genes (i.e., $Y_{n \times g}$) as a combination of annotated and unannotated factors as follows:

$$Y_{n \times g} = C_{n \times p}\beta_{p \times 1} + F_{n \times f}A_{f \times g} + U_{n \times u}H_{u \times g} + \varepsilon_{n \times g}$$

Where:

$Y_{n \times g}$ represents the observed data matrix, typically with dimensions $n \times g$ (where n is the number of samples or cells and g is the number of variables or genes)

$C_{n \times p}$ is the matrix of technical covariates with dimensions $n \times p$ (where p is the number of covariates), such as library size, batch ID, cell cycle stage

$\beta_{p \times 1}$ represents the coefficient vector for technical covariates with dimensions $p \times 1$

$F_{n \times f}$ is the matrix of annotated factors with dimensions $n \times f$ (where f is the number of factors)

$A_{f \times g}$ is the matrix of loadings for annotated factors with dimensions $f \times g$

$U_{n \times u}$ is the matrix of unannotated factors with dimensions $n \times u$ (where u is the number of unannotated factors)

$H_{u \times g}$ represents the matrix of loadings for unannotated factors with dimensions $u \times g$

$\varepsilon_{n \times g}$ is the error term, with dimensions $n \times g$

Annotated factors are those matched with known (given) covariates as indicated in the factor-covariate association (FCA) table. The solution to the above equation is reached through a two-step process.

1. Derivation of residuals
The first step aims to remove the effect of technical covariates from the data.

Input counts, represented by the matrix $Y_{n \times g}$ are modeled as a Poisson generalized linear model (GLM) to account for the matrix's distributional properties[11,53,55]. Technical covariates $C_{n \times p}$ are incorporated into the model to capture their effects on the count data. The statsmodels package[56] (version 0.11.0) is used for GLM implementation.

Pearson residuals from this model are computed as the difference between observed and predicted counts divided by the square root of the predicted counts:

$$r_i = \frac{y_i - \hat{y}_i}{\sqrt{\mathrm{VAR}(\hat{y}_i)}}$$

where VAR is the variance. For Poisson GLM, $\mathrm{VAR}(\hat{y}_i) = \hat{y}_i$

The Pearson residuals are used for subsequent matrix decomposition.

Two additional residual types were evaluated, but not used in sciRED. Response residuals represent the difference between the observed count and the predicted mean count for each observation.
Response Residuals: $resid_i = y_i - \hat{y}_i$

Deviance residuals represent the individual contributions of samples to the deviance D, calculated as the signed square roots of the unit deviances. Deviance Residuals:

$$d_i = \mathrm{sign}(y_i - \hat{y}_i) \times \sqrt{2 \times (y_i \log(y_i/\hat{y}_i) - (y_i - \hat{y}_i))}$$

Pearson residuals are used for sciRED because they are established in other single cell analysis methods[53,54]. However, sciRED results are robust to the choice of residual (among Pearson, response, deviance) (See method section "Classifier ensemble").

2. Residual decomposition

After obtaining Pearson residuals from the count data, a matrix factorization technique is employed to uncover underlying patterns, including the annotated and unannotated factors. PCA factors are calculated using Singular Value Decomposition (SVD)[57] as implemented in scikit-learn[58] (version 0.22.1). Following factor decomposition, we apply varimax rotation to enhance the interpretability of the principal axes in the feature space. To achieve this we reimplemented the optimized estimation procedure as described below.

Rotation types

Factor analysis typically comprises two sequential stages. Initially, loadings are computed to best approximate the observed variances within the data. However, these initial loadings may lack interpretability, thus we apply rotation to generate a revised set that is more easily interpretable. There are two primary rotation types in factor analysis: orthogonal and oblique rotations. Orthogonal rotation, such as varimax, seeks to produce orthogonal factors with zero correlations. Intuitively, varimax rotation aims to identify factors associated with a limited number of variables, thereby it promotes the detection of distinct factors rather than those affecting all variables evenly. Mathematically, interpretability is achieved by maximizing the variance of the squared loadings along each principal component axis. Varimax rotation seeks to maximize the Kaiser criterion:

$$v = \sum_j v_j = \sum_j \left\{ \left[g \sum_i \left(l_{ij}^2/h_i^2 \right)^2 - \left(\sum_i l_{ij}^2/h_i^2 \right)^2 \right] / g^2 \right\}$$

Where v is the Kaiser criterion and l_{ij} is the loading value of ith gene and jth factor, and g is the total number of genes. The communality h_i is calculated as the squared sum of the loading values for each gene.

$$h_i^2 = \sum_j l_{ij}^2$$

To explicitly specify the rotation matrix, we can reformulate the Kaiser criterion using the following notation. Let L be a $g \times k$ loading matrix (eigenvectors), and R denote a rotation matrix such that $R^T R = I_k$, where I_k is the $k \times k$ identity matrix. Additionally, let R_{ij} represent the scalar element in the ith row and jth column of matrix R. Varimax rotations can now be described as follows:

$$\mathbf{R}_{\text{varimax}} = \arg\max_{\mathbf{R}} \left(\sum_{j=1}^{k} \sum_{i=1}^{g} (\mathbf{LR})_{ij}^4 - \frac{1}{g} \sum_{j=1}^{k} \left(\sum_{i=1}^{g} (\mathbf{LR})_{ij}^2 \right)^2 \right)$$

where R_{varimax} denotes the resulting rotation matrix.

The rotation matrix is computed using an iterative method relying on SVD to achieve sparsity in the loadings. Subsequently, the rotated loadings and score matrices are derived by multiplying the original loadings and score matrices with the rotation matrix, respectively. The optimization algorithm is elaborated on in detail in Appendix A of Stegmann *et al.*[59]. We re-implemented the base R varimax rotation function in Python.

Oblique rotations, such as promax, allow factors to be correlated, thereby relaxing the orthogonality assumption[60]. This flexibility can be beneficial when factors are expected to be correlated within the

underlying structure of the data. Promax initially applies the varimax method to generate a set of orthogonal results. Subsequently, it constructs an ideal oblique solution to exaggerate the orthogonal rotated gene-loading matrix. Finally, it rotates the orthogonal results to achieve a least squares fit with this ideal solution.

We define a pattern matrix $P = (p_{ij})$, as the following ($k > 1$):

$$p_{ij} = \frac{\left|l_{ij}^{k+1}\right|}{l_{ij}}$$

Each element of P matrix is the kth power (typically 3rd power) of the corresponding element in the row-column normalized varimax loading matrix. Next, the least squares fit of the orthogonal matrix of factor loadings to the pattern matrix is computed.

$$R_{\text{Promax}} = \underset{R}{\text{argmin}} \|P - L_{\text{rot}} R\|_2$$
$$R_{\text{Promax}} = (L'_{\text{rot}} L_{\text{rot}})^{-1} L'_{\text{rot}} P$$

where R_{Promax} is the unnormalized rotation matrix, L_{rot} is the varimax rotated loadings, and P is the pattern matrix defined above. The columns of R_{Promax} are normalized such that their sums of squares are equal to unity. We reimplemented the base R promax function in Python.

To evaluate the impact of factor rotations, we applied PCA, sciRED (varimax-based[18]), and promax-rotated[61] PCA to the Pearson residual of the SCMixology dataset after regressing out protocol and library size. The factor-covariate association scores reveal a high correlation between sciRED and Promax. Both methods enhance specificity and achieve one-to-one association between factors and cell line covariates, outperforming unrotated PCA (Figure S6). We used varimax as the default rotation method for sciRED, as it has been established to perform well for interpretable factor analysis [62,63].

Feature importance calculation

We evaluated a range of classifiers for inclusion in the sciRED ensemble classifier. Each classifier is trained on individual levels of each covariate separately (e.g. "female" and "male" for a "biological sex" covariate). Each classifier uses a different approach to estimate feature importance:

1) Logistic regression: feature importance is the magnitude of the coefficient for each factor, which represents the change in the log-odds of belonging to a covariate level per unit of factor weight.

2) Decision trees, random forest[64] and extreme gradient boosting: feature importance scores represent the decrease in covariate mixing (e.g. Gini impurity or entropy) when the feature is used within a tree averaged across all trees.

3) K-nearest neighbor[65] (KNN): feature importance is estimated as the decrease in predictive accuracy when the values for that feature are randomly permuted. This value is calculated as the average across five permutations for each factor based on the default scikit-learn package implementation.

4) Linear classifier (AUC): feature importance for a linear classifier (i.e. fixed threshold) is calculated as the area under (AUC) the receiver-operating characteristic (ROC) curve. The

AUC for one-dimensional data is equivalent to the Wilcoxon or Mann-Whitney U test statistic with the relation:

$$\text{AUC} = \frac{U}{n_0 \times n_1}$$

Where U is the Mann-Whitney U statistic, and n_0 and n_1 are the sample sizes of the two groups being compared. Mann-Whitney U test is a non-parametric test used to assess whether two independent samples are selected from populations having the same mean rank. Here, samples are defined as factor scores for the target group (cells labeled with the covariate level of interest) and the non-target group. In the context of feature importance, a higher AUC value indicates that the factor is better at separating the classes, while a lower AUC value suggests less discriminatory power. The scikit-learn package is used to implement decision tree, random forest, logistic regression and KNN classifiers with default parameters. XGBoost (version 1.5.0) and scipy[66] (version 1.4.1) packages are used for XGB and the Mann-Whitney U test, respectively.

Classifier ensemble

We optimized the sciRED classifier ensemble by evaluating different classifier combinations on four independent datasets: a healthy human kidney map, a healthy human liver map, a PBMC atlas, and the scMixology benchmark dataset (Figure S7). For each experiment, we randomly shuffled the covariate labels to generate a null distribution of classifier association scores and calculated the average number of significant associated factors (p < 0.05) per covariate level (Figure S7A). We defined a one-to-one association between factors and covariates as the optimally interpretable result. This analysis shows that the sciRED classifier (ensemble of logistic regression, linear classifier/area under the curve (AUC), decision tree and extreme gradient boosting (XGB)) outperforms or matches the performance of the individual classifiers, depending on the data set. Initially, six classifiers—AUC, K-Nearest Neighbors (KNN), logistic regression, decision tree, random forest, and XGB—were compared on the scMixology benchmark dataset. Due to KNN's poor classification performance and the random forest's inferior scalability, they were excluded from the sciRED ensemble model (Figures S7BC). Benchmarking on the four independent datasets described above demonstrates sciRED's superior performance relative to single classifiers (Figures 7D-G).

To optimize the ensemble score, we also tested all combinations of three different scaling methods and two mean calculations (Figure S8). Specifically, we considered standardization, min-max scaling, or rank-based scaling combined with arithmetic or geometric means[67]. By comparing scores for the real scMixology data vs. permuted data labels, we identified standardization followed by arithmetic mean calculation as the optimal scoring method (Figure S8).

The standardization, min-max scaling, and rank-based scaling are defined as follows:

Given a set of feature importance scores for each factor $i : x = \{x_1, x_2, \ldots, x_n\}$, and their ascending order of ranks $r = \{r_1, r_2, \ldots, r_n\}$, where n is the total number of features (factors):

$$\text{standardized}_i = \frac{x_i - \text{mean}(x)}{\text{std}(x)}$$

$$\text{min-max scaled}_i = \frac{x_i - \min(x)}{\max(x) - \min(x)}$$

$$\text{rank-scaled}_i = \frac{r_i}{n}$$

Rank scaling generates a value between 0 and 1 to each data point based on its rank within the dataset. Lower values in the original dataset will have lower rank-based scaled values, while higher values will have higher rank-based scaled values.

Arithmetic and geometric means across classifiers are calculated as follows:

$$\text{Arithmetic mean} = \frac{1}{n} \sum_{i=1}^{n} x_i$$

Where n is the number of values.

$$\text{Geometric mean} = \left(\prod_{i=1}^{n} x_i \right)^{\frac{1}{n}}$$

The geometric mean is the nth root of the product of a set of values.

The effect of the choice of residual (Pearson, response, deviance) on sciRED performance was also evaluated, indicating that sciRED results are robust to the choice of residual (Figure S9).

Determining significant factor-covariate associations
FCA scores are binarized into significant and non-significant associations based on a threshold. This threshold is automatically determined using Otsu thresholding[68]. Otsu thresholding iterates through all potential threshold values and computes a separability measure in each iteration. The threshold value that maximizes this separability measure is chosen as the optimal threshold to partition the FCA score distributions into significant and non-significant associations. scikit-image package[69] (version 0.23.2) is used for implementation.

Benchmarking covariate-factor association metrics based on permutation results
We used a permutation test to evaluate the significance of each covariate-factor association. This process entailed randomly shuffling cell covariate labels 500 times and recalculating factor-covariate association scores for each permutation to create an empirical null distribution. A shuffled dataset should result in lower-scaled factor-covariate association scores compared to the original dataset, given that the cell labels are randomized after each permutation.

Empirical p-values were calculated as the number of permuted FCA scores are as or more extreme than the observed association value divided by the number of permutations. The number of significant associations for each covariate was determined using p-value < 0.05. We expect one significant factor association per covariate level in the ideal case. High values of this metric likely indicate false positive associations (low specificity) and zero values highlight false negative results (low sensitivity).

To evaluate model performance without relying on predefined thresholds (such as p-value=0.05), we employed the Gini index, an inequality measure ranging from 0 to 1. A Gini index of 0 signifies perfect equality, where all values are identical, while a score of 1 indicates perfect inequality, with one value

dominating the distribution. In our context, we aimed to assess the extent of association between factors and covariates across various levels of pre- and post-permutation. Following label shuffling, we expect the factor-covariate association scores to exhibit uniformity across all covariate levels (Gini score closer to 0). In cases of non-random baseline labels, sparse associations between factors and covariates would result in a Gini score closer to 1. To calculate the Gini index for a given FCA matrix, Gini was calculated for each covariate level separately and the average Gini index across all covariate levels is provided.

$$G_k = \frac{1}{2n^2\bar{x}} \sum_{i=1}^{n} \sum_{j=1}^{n} |x_i - x_j|$$

Where G_k is the Gini coefficient for a covariate level k, n is the number of factors, and $\bar{x}$ are the mean FCA scores for a given covariate level. We then calculate the global Gini index as:

$$G = \frac{1}{K} \sum_{i=1}^{K} G_k$$

Where K is the total number of covariate levels.

Factor evaluation

We defined four categories of metrics: separability, effect size, specificity, and homogeneity to measure factor interpretability. Two are label-free (separability, effect size) and the other two are label-dependent (specificity, and homogeneity). Metrics for each category are organized into a table of factor interpretability scores (FIS), with metrics arranged as rows and factors as columns. Subsequently, the FIS undergoes a row-wise scaling and is visualized as a heatmap to support comparison of interpretability scores between factors.

sciRED uses the Silhouette score and bimodality index to assess separability. Homogeneity is measured using the arithmetic mean of the average scaled variance (ASV) table. The Simpson index is employed to evaluate factor specificity, while factor variance serves as an effect size measure (Figure S10, See method section "Correlation between interpretability metrics and overlap values").

Separability (bimodality)

We use bimodality scores as an indicator for measuring the separability of factors. We use existing metrics developed for identifying genes with bimodal expression distributions, which are typically used to identify genes with prognostic value in discriminating patient subgroups. We selected metrics in accordance with Hellwig et al.'s comparative assessment of these scores based on survival times in a breast cancer dataset[70].

Cluster-based bimodality measures

Cluster-based methods group observations into clusters then calculate various statistics to measure the degree of distinctiveness of these clusters. Clusters were generated using a standard k-means [71] algorithm (k=2) implemented using the scikit-learn[58] package. The following cluster-based bimodality measures are included in sciRED:

- Variance Ratio Score (VRS) also known as Calinski–Harabasz index (CHI)[72] assesses the proportion of variance reduction when splitting the data into two clusters. We can decompose the total sum of squares (TSS) to between-cluster sum of squares (BSS) and within-cluster sum of squares (WSS). VRS is then defined as the ratio of BSS and WSS.

- Weighted Variance Ratio score (WVRS) is similar to VRS but measures the variance reduction independent of the cluster sample sizes. In both cases, higher values indicate better separation between clusters and reflect bimodality.
- Silhouette score[73] measures the cohesion and separation of clusters, ranging from -1 to 1, where higher values indicate better-defined clusters. Silhouette is calculated based on mean intra-cluster distance (ICD) and the mean nearest-cluster distance (NCD). For each data point Silhouette is then given as (NCD - ICD)/max(ICD, NCD).
- Davies-Bouldin index[74] computes the average similarity between each cluster and its most similar cluster. It measures similarity as the ratio of within-cluster distances to between-cluster distances. The minimum value is zero with lower values indicating better cluster separation. To ensure consistency with other metrics, we scale the inverse Davies-Bouldin Index.

Calinski–Harabasz, Silhouette and Davies-Bouldin Indices were implemented using scikit-learn.

Bimodality index
The Bimodality Index[75] is another bimodality metric which has initially been introduced to rank bimodal gene expression signatures within cancer gene expression datasets. We adopt the bimodality index to assess the bimodal nature of factor scores by modeling them as a mixture of two normal distributions using a Gaussian Mixture Model (GMM). Let μ_1 and μ_2 represent the means of the two normal distributions, and σ the standard deviation. Given an equal variance assumption, the standardized distance δ between the distributions is calculated by:

$$\delta = \frac{|\mu_1 - \mu_2|}{\sigma}$$

Given GMM estimated parameters, we can calculate the proportion of observations in the first component π. We then compute the bimodality index (BI) as:

$$\mathrm{BI} = \sqrt{\pi(1-\pi)} \times \delta$$

A higher BI indicates a stronger bimodal distribution, aiding in the identification of bimodal factor signatures. Scikit-learn was used to fit GMMs.

Dip score
Another bimodality evaluation metric is Hartigan's dip test[76], a statistical measure used to assess deviations from unimodality in distributions. It evaluates multimodality by comparing the maximum difference between the empirical distribution function and the unimodal distribution function that minimizes this difference. The dip score was computed for each factor, indicating the degree of bimodality present in the factor distribution. Higher dip scores suggest stronger evidence of bimodality, while lower scores indicate unimodality. Implementation was based on the diptest package.

Effect size
The variance of factor scores across cells was employed as a measure of effect size consistency.

Specificity

We assessed the Simpson diversity index and Shannon entropy as measures of specificity.

Simpson diversity Index

The Simpson diversity index is a measure commonly used in ecology to quantify the diversity or evenness of species within a community[77]. It assesses the probability of encountering different species within a community and how evenly distributed these species are. We adopted the Simpson diversity index to measure specificity for individual factors within the context of FCA scores. By applying the Simpson index to each vector of FCA scores, we can evaluate the extent to which a factor uniquely characterizes a particular covariate level.

Mathematically, the Simpson diversity index D is expressed as

$$D = \sum_{i=1}^{n} p_i^2$$

where p_i denotes the scaled score of factor-covariate level association (probability of a factor being chosen for a given covariate level i), and n represents the total number of covariate levels. Here, the Simpson diversity index ranges between 0 and 1, where 0 indicates low factor specificity (maximum diversity, all factor association scores are equally distributed) and 1 indicates greater specificity (minimum diversity) of a factor towards a particular covariate level.

Shannon diversity index

We applied Shannon entropy to measure the specificity of individual factors within FCA scores. By calculating Shannon entropy for each vector of FCA scores, we assess how uniquely a factor characterizes a particular covariate level.

Mathematically, Shannon entropy is defined as:
$$H = -\sum_{i=1}^{N} p_i \log(p_i)$$

where p_i is the probability of a factor being associated with a given covariate level i, and N is the total number of covariate levels. Shannon diversity index ranges from 0 (high factor specificity) to $\log(N)$ (low factor specificity).

Homogeneity

To assess the homogeneity or even distribution of factor scores across different levels of a covariate, we compute the scaled variance for each covariate level. This metric quantifies the proportion of variance in the factor scores observed at a specific covariate level (L) relative to the total variance across all covariate levels[78]. Thus, the scaled variance SV for a factor x and a particular covariate level L is computed as

$$SV = \frac{\mathrm{Var}(x_L)}{\mathrm{Var}(x)}$$

Here, $\mathrm{Var}(x_L)$ denotes the variance of the factor scores x corresponding to the covariate level L, and $\mathrm{Var}(x)$ represents the total variance of the factor scores across all cells.

To establish a unified metric across all levels of a single covariate (e.g., Batch1, Batch2, etc., representing levels of the covariate "Batch"), we adopt different approaches based on the covariate's number of unique levels. We compute both the geometric and arithmetic means of the scaled variances (SV) of all covariate levels for each factor. The arithmetic mean of SV values was chosen based on factor simulation results showing it performed best (explained below).

Evaluating factor interpretability metrics using simulation
Simulating mixture Gaussian distribution
Factors were simulated under the assumption of being generated from a mixture of Gaussian distributions. Each Gaussian distribution represents the factor scores of the cells belonging to one covariate level. This simulation process was implemented using the following mathematical formulation:

Let X be a random variable representing the simulated factors. We generated n samples (cells) from a mixture of K (K=2) normal distributions, each characterized by its mean μ_k, standard deviation σ_k, and proportion p_k. The mixture distribution X follows the distribution:
$$\sum_{k=1}^{K} p_k \cdot \mathcal{N}(\mu_k, \sigma_k^2)$$

where $\mathcal{N}(\mu_k, \sigma_k^2)$ denotes the probability density function (PDF) of the k-th normal distribution.
Given this assumption, 10 factors for 10000 cells were simulated for 100 rounds. p_k was set to 0.5 for simplicity. μ and σ were set by random sampling from uniform distributions (parameters: $\sigma_{\min}$=0.5, $\sigma_{\max}$=1, $\mu_{\min}$=0, $\mu_{\max}$=4).

Correlation between interpretability metrics and overlap values
We assessed the efficacy of the proposed factor interpretability metrics by examining their correlation with the overlap between the two Gaussian distributions representing each factor. We anticipated that factors exhibiting greater overlap would demonstrate lower separability and specificity scores (negative correlation), along with higher homogeneity values (positive correlation), and vice versa. Our goal was to identify metrics with higher absolute mean correlation values and lower variability, as illustrated in Figures S10A and S10B. Based on simulation results (Figure S10C), Silhouette and bimodality index indicate high performance for the separability measure. The arithmetic mean of the average scaled variance (ASV) table shows higher performance compared to the geometric mean for the homogeneity measure. Our simulation results indicated a superior performance of simpson index compared to Shannon entropy[79] to measure factor specificity.

Calculating overlap between double Gaussian distributions:
The overlap between two Gaussian distributions with means μ_1 and μ_2, and standard deviations σ_1 and σ_2 respectively, is quantified based on the intersection of the PDFs of the two distributions. For distributions with unequal means and standard deviations, the overlap O is computed as:
$$O = 1 - \frac{1}{2}\left[\text{erf}\left(\frac{c - \mu_1}{\sqrt{2}\sigma_1}\right) - \text{erf}\left(\frac{c - \mu_2}{\sqrt{2}\sigma_2}\right)\right]$$
where c represents the intersection point of the two PDFs and erf is the error function.

Pathway and gene set enrichment analysis

Gene set and pathway enrichment analysis methods were used to study the biological signatures represented by each factor. The gene scores corresponding to the factors of interest were selected from the loading matrix to order the list of genes from most to least contribution to the given factor. Pathway enrichment analysis was performed on the top 200 genes of the ordered loadings using the gprofiler2[80] (version 0.2.3) enrichment tool based on the default Gene Ontology Biological Process and Reactome gene set database sources, and using the "ranked" mode.

Data preprocessing

Scmixology

The scMixology[24] dataset includes three human lung adenocarcinoma cell lines: HCC827, H1975, and H2228. These cell lines were cultured individually and subsequently processed. Single cells from each cell line were combined in equal proportions and libraries were generated using three protocols: CEL-seq2, Drop-seq, and 10X Chromium. The processed count data was obtained using the scPipe package in R and converted to .h5ad for import into Python. The data underwent log normalization and standardization using the "StandardScaler" function from scikit-learn package.

Interferon (IFN)-β stimulated PBMC dataset

The stimulated data was downloaded from muscData package (Kang18_8vs8, GEO: GSE96583)[26] . This dataset includes 10x Genomics droplet-based scRNA-seq PBMC data from eight lupus patients before and after 6h-treatment with interferon-beta. Count data was extracted, and analyzed using sciRED (number of components(k)=30) while modeling library size as a technical covariate. Three outlier cells were removed from the sciRED cell-by-factor score matrix, and factors F2 and F9 scores for 29,062 cells were visualized in Figure 3.

Healthy human kidney atlas

The healthy human kidney map was constructed based on 19 living donors (10 female, 9 male)[25] including the transcriptomes of 27,677 cells. The processed files were downloaded from the UCSC Cell Browser [https://cells.ucsc.edu/?ds=living-donor-kidney]. Filtered and normalized data was downloaded and analyzed using sciRED (k=30).

Healthy rat liver atlas

The healthy rat total liver homogenate map includes four whole livers which were acquired from 8-10 week-old healthy male Dark Agouti and Lewis strain rats, and the resulting total liver homogenates went through two-step collagenase digestion and 10x droplet-based scRNA-seq[27]. The processed healthy rat liver total homogenate map was downloaded from the UCSC Cell Browser [https://cells.ucsc.edu/?ds=rat-liver-atlas] (GEO: GSE220075). Five outlier cells were removed from the score matrix, and factors F6 and F20 scores for 23,036 cells were visualized in Figure 4. sciRED (k=30) was applied to the count data while modeling library size as a technical covariate. Sample was not included as technical covariate to preserve the strain-specific variations. SoupX[29] software (version: 1.6.2) was used to identify genes with the greatest contribution to the ambient RNA. We used the default automatic contamination fraction estimation (Rho) feature in the SoupX (autoEstCont function) to estimate Rho for each sample included in the total liver homogenate map of healthy rat livers. Subsequently, we extracted the estimated ambient RNA profile and identified the top 50 genes contributing the most to the ambient RNA in each sample. Genes were selected if they ranked among

the high-scoring ambient RNA contributors in at least two samples. These selected genes were assessed for their presence among the strain-specific myeloid markers identified using both sciRED and standard differential expression methods. Differential expression analysis between the DA and LEW strains within the myeloid population (cluster 5) of the rat liver map was conducted using Seurat's FindMarkers function with default parameters (logfc.threshold = 0.1, min.pct = 0.01, min.cells.feature = 3, and min.cells.group = 3), implementing the non-parametric Wilcoxon rank-sum test.

Healthy Human Liver Atlas

The healthy human liver map[30] includes 8,444 parenchymal and non-parenchymal cells obtained from the fractionation of fresh hepatic tissue from five human livers. The liver tissue was obtained from livers procured from deceased donors deemed acceptable for liver transplantation. Data was downloaded from the R package HumanLiver, available at https://github.com/BaderLab/HumanLiver, and sciRED (k=30) was applied to filtered count while modeling library size as a technical covariate.

Method availability

A Python package for sciRED with example case scenarios is freely available from: https://github.com/delipouya/sciRED

References

1. Leek, J. T. & Storey, J. D. Capturing heterogeneity in gene expression studies by surrogate variable analysis. *PLoS Genet.* **3**, 1724–1735 (2007).
2. Lähnemann, D. *et al.* Eleven grand challenges in single-cell data science. *Genome Biol.* **21**, 31 (2020).
3. Eisen, M. B., Spellman, P. T., Brown, P. O. & Botstein, D. Cluster analysis and display of genome-wide expression patterns. *Proc Natl Acad Sci USA* **95**, 14863–14868 (1998).
4. Luecken, M. D. & Theis, F. J. Current best practices in single-cell RNA-seq analysis: a tutorial. *Mol. Syst. Biol.* **15**, e8746 (2019).
5. Pearson, K. On lines and planes of closest fit to systems of points in space. *Philosophical Magazine Series 6* **2**, 559–572 (1901).
6. Lee, D. D. & Seung, H. S. Learning the parts of objects by non-negative matrix factorization. *Nature* **401**, 788–791 (1999).
7. Jutten, C. & Herault, J. Blind separation of sources, part I: An adaptive algorithm based on neuromimetic architecture. *Signal Processing* **24**, 1–10 (1991).
8. Comon, P. Independent component analysis, A new concept? *Signal Processing* **36**, 287–314 (1994).
9. Risso, D., Perraudeau, F., Gribkova, S., Dudoit, S. & Vert, J.-P. A general and flexible method for signal extraction from single-cell RNA-seq data. *Nat. Commun.* **9**, 284 (2018).
10. Pierson, E. & Yau, C. ZIFA: Dimensionality reduction for zero-inflated single-cell gene expression analysis. *Genome Biol.* **16**, 241 (2015).
11. Townes, F. W., Hicks, S. C., Aryee, M. J. & Irizarry, R. A. Feature selection and dimension reduction for single-cell RNA-Seq based on a multinomial model. *Genome Biol.* **20**, 295 (2019).
12. Kotliar, D. *et al.* Identifying gene expression programs of cell-type identity and cellular activity with single-cell RNA-Seq. *eLife* **8**, (2019).
13. Stein-O'Brien, G. L. *et al.* Decomposing Cell Identity for Transfer Learning across Cellular

Measurements, Platforms, Tissues, and Species. *Cell Syst.* **8**, 395-411.e8 (2019).

14. Buettner, F. *et al.* Computational analysis of cell-to-cell heterogeneity in single-cell RNA-sequencing data reveals hidden subpopulations of cells. *Nat. Biotechnol.* **33**, 155–160 (2015).

15. Buettner, F., Pratanwanich, N., McCarthy, D. J., Marioni, J. C. & Stegle, O. f-scLVM: scalable and versatile factor analysis for single-cell RNA-seq. *Genome Biol.* **18**, 212 (2017).

16. Kunes, R. Z., Walle, T., Land, M., Nawy, T. & Pe'er, D. Supervised discovery of interpretable gene programs from single-cell data. *Nat. Biotechnol.* **42**, 1084–1095 (2024).

17. Nelder, J. A. & Wedderburn, R. W. M. Generalized Linear Models. *J. R. Stat. Soc. Ser. A* **135**, 370 (1972).

18. Kaiser, H. F. The varimax criterion for analytic rotation in factor analysis. *Psychometrika* **23**, 187–200 (1958).

19. Cox, D. R. The regression analysis of binary sequences. *Journal of the Royal Statistical Society: Series B (Methodological)* **20**, 215–232 (1958).

20. Bamber, D. The area above the ordinal dominance graph and the area below the receiver operating characteristic graph. *J. Math. Psychol.* **12**, 387–415 (1975).

21. Fawcett, T. An introduction to ROC analysis. *Pattern Recognit. Lett.* **27**, 861–874 (2006).

22. Wu, X. *et al.* Top 10 algorithms in data mining. *Knowl. Inf. Syst.* **14**, 1–37 (2008).

23. Chen, T. & Guestrin, C. XGBoost: A Scalable Tree Boosting System. in *Proceedings of the 22nd ACM SIGKDD International Conference on Knowledge Discovery and Data Mining - KDD '16* 785–794 (ACM Press, 2016). doi:10.1145/2939672.2939785.

24. Tian, L. *et al.* Benchmarking single cell RNA-sequencing analysis pipelines using mixture control experiments. *Nat. Methods* **16**, 479–487 (2019).

25. McEvoy, C. M. *et al.* Single-cell profiling of healthy human kidney reveals features of sex-based transcriptional programs and tissue-specific immunity. *Nat. Commun.* **13**, 7634 (2022).

26. Kang, H. M. *et al.* Multiplexed droplet single-cell RNA-sequencing using natural genetic variation. *Nat. Biotechnol.* **36**, 89–94 (2018).

27. Pouyabahar, D. *et al.* A rat liver cell atlas reveals intrahepatic myeloid heterogeneity. *iScience* **26**, 108213 (2023).

28. Andrews, T. S. *et al.* Single cell, single nucleus and spatial RNA sequencing of the human liver identifies hepatic stellate cell and cholangiocyte heterogeneity. *BioRxiv* (2021) doi:10.1101/2021.03.27.436882.

29. Young, M. D. & Behjati, S. SoupX removes ambient RNA contamination from droplet-based single-cell RNA sequencing data. *Gigascience* **9**, giaa151. (2020).

30. MacParland, S. A. *et al.* Single cell RNA sequencing of human liver reveals distinct intrahepatic macrophage populations. *Nat. Commun.* **9**, 4383 (2018).

31. Andrews, T. S. *et al.* Single-cell, single-nucleus, and spatial transcriptomics characterization of the immunological landscape in the healthy and PSC human liver. *J. Hepatol.* **80**, 730–743 (2024).

32. Halpern, K. B. *et al.* Single-cell spatial reconstruction reveals global division of labour in the mammalian liver. *Nature* **542**, 352–356 (2017).

33. Nicolau-Neto, P. *et al.* UBE2C is a transcriptional target of the cell cycle regulator FOXM1. *Genes* **9**, (2018).

34. Wang, T., Lu, J., Wang, R., Cao, W. & Xu, J. TOP2A promotes proliferation and metastasis of hepatocellular carcinoma regulated by miR-144-3p. *J. Cancer* **13**, 589–601 (2022).

35. Huang, L. *et al.* KPNA2 promotes cell proliferation and tumorigenicity in epithelial ovarian

carcinoma through upregulation of c-Myc and downregulation of FOXO3a. *Cell Death Dis.* **4**, e745 (2013).

36. Martinsson-Ahlzén, H.-S. *et al.* Cyclin-dependent kinase-associated proteins Cks1 and Cks2 are essential during early embryogenesis and for cell cycle progression in somatic cells. *Mol. Cell. Biol.* **28**, 5698–5709 (2008).

37. Xu, L., Yu, W., Xiao, H. & Lin, K. BIRC5 is a prognostic biomarker associated with tumor immune cell infiltration. *Sci. Rep.* **11**, 390 (2021).

38. Cao, Y., Yang, P. & Yang, J. Y. H. A benchmark study of simulation methods for single-cell RNA sequencing data. *Nat. Commun.* **12**, 6911 (2021).

39. Zappia, L., Phipson, B. & Oshlack, A. Splatter: simulation of single-cell RNA sequencing data. *Genome Biol.* **18**, 174 (2017).

40. Li, W. V. & Li, J. J. A statistical simulator scDesign for rational scRNA-seq experimental design. *Bioinformatics* **35**, i41–i50 (2019).

41. Vieth, B., Ziegenhain, C., Parekh, S., Enard, W. & Hellmann, I. powsimR: power analysis for bulk and single cell RNA-seq experiments. *Bioinformatics* **33**, 3486–3488 (2017).

42. Baruzzo, G., Patuzzi, I. & Di Camillo, B. SPARSim single cell: a count data simulator for scRNA-seq data. *Bioinformatics* **36**, 1468–1475 (2020).

43. Zhang, X., Xu, C. & Yosef, N. Simulating multiple faceted variability in single cell RNA sequencing. *Nat. Commun.* **10**, 2611 (2019).

44. Stein-O'Brien, G. L. *et al.* Enter the Matrix: Factorization Uncovers Knowledge from Omics. *Trends Genet.* **34**, 790–805 (2018).

45. Revelle, W. psych: Procedures for Psychological, Psychometric, and Personality Research. (2024).

46. Waller, N. simFA: A Program for Exploring Factor Analysis Models Through Monte Carlo Simulations. (2021).

47. Briggs, N. E. & MacCallum, R. C. Recovery of weak common factors by maximum likelihood and ordinary least squares estimation. *Multivariate Behav. Res.* **38**, 25–56 (2003).

48. Cliff, N. & Pennell, R. The influence of communality, factor strength, and loading size on the sampling characteristics of factor loadings. *Psychometrika* **32**, 309–326 (1967).

49. Lopez, R., Regier, J., Cole, M. B., Jordan, M. I. & Yosef, N. Deep generative modeling for single-cell transcriptomics. *Nat. Methods* **15**, 1053–1058 (2018).

50. Svensson, V., Gayoso, A., Yosef, N. & Pachter, L. Interpretable factor models of single-cell RNA-seq via variational autoencoders. *Bioinformatics* **36**, 3418–3421 (2020).

51. Choi, Y., Li, R. & Quon, G. siVAE: interpretable deep generative models for single-cell transcriptomes. *Genome Biol.* **24**, 29 (2023).

52. Gastwirth, J. L. The estimation of the lorenz curve and gini index. *Rev. Econ. Stat.* **54**, 306 (1972).

53. Lause, J., Berens, P. & Kobak, D. Analytic Pearson residuals for normalization of single-cell RNA-seq UMI data. *Genome Biol.* **22**, 258 (2021).

54. Hafemeister, C. & Satija, R. Normalization and variance stabilization of single-cell RNA-seq data using regularized negative binomial regression. *Genome Biol.* **20**, 296 (2019).

55. Pan, Y. *et al.* The Poisson distribution model fits UMI-based single-cell RNA-sequencing data. *BMC Bioinformatics* **24**, 256 (2023).

56. Seabold, S. & Perktold, J. Statsmodels: Econometric and Statistical Modeling with Python. in *Proceedings of the 9th Python in Science Conference* 92–96 (SciPy, 2010). doi:10.25080/Majora-92bf1922-011.

57. Klema, V. & Laub, A. The singular value decomposition: Its computation and some applications. *IEEE Trans. Automat. Contr.* **25**, 164–176 (1980).

58. Varoquaux, G. *et al.* Scikit-learn. *GetMobile: Mobile Comp. and Comm.* **19**, 29–33 (2015).

59. Stegmann, M. B., Sjöstrand, K. & Larsen, R. Sparse modeling of landmark and texture variability using the orthomax criterion. in *Medical Imaging 2006: Image Processing* (eds. Reinhardt, J. M. & Pluim, J. P. W.) vol. 6144 61441G (SPIE, 2006).

60. Dien, J., Khoe, W. & Mangun, G. R. Evaluation of PCA and ICA of simulated ERPs: Promax vs. Infomax rotations. *Hum. Brain Mapp.* **28**, 742–763 (2007).

61. Hendrickson, A. E. & White, P. O. PROMAX: A QUICK METHOD FOR ROTATION TO OBLIQUE SIMPLE STRUCTURE. *British Journal of Statistical Psychology* **17**, 65–70 (1964).

62. Akhtar-Danesh, N. Impact of factor rotation on Q-methodology analysis. *PLoS ONE* **18**, e0290728 (2023).

63. Darton, R. A. Rotation in factor analysis. *The Statistician* **29**, 167 (1980).

64. Tin Kam Ho. Random decision forests. in *Proceedings of 3rd International Conference on Document Analysis and Recognition* 278–282 (IEEE Comput. Soc. Press, 1995). doi:10.1109/ICDAR.1995.598994.

65. Cover, T. & Hart, P. Nearest neighbor pattern classification. *IEEE Trans. Inform. Theory* **13**, 21–27 (1967).

66. Virtanen, P. *et al.* SciPy 1.0: fundamental algorithms for scientific computing in Python. *Nat. Methods* **17**, 261–272 (2020).

67. Mitchell, D. W. 88.27 More on spreads and non-arithmetic means. *The Mathematical Gazette* **88**, 142–144 (2004).

68. Otsu, N. A Threshold Selection Method from Gray-Level Histograms. *IEEE Trans. Syst. Man Cybern.* **9**, 62–66 (1979).

69. van der Walt, S. *et al.* scikit-image: image processing in Python. *PeerJ* **2**, e453 (2014).

70. Hellwig, B. *et al.* Comparison of scores for bimodality of gene expression distributions and genome-wide evaluation of the prognostic relevance of high-scoring genes. *BMC Bioinformatics* **11**, 276 (2010).

71. Lloyd, S. Least squares quantization in PCM. *IEEE Trans. Inform. Theory* **28**, 129–137 (1982).

72. Calinski, T. & Harabasz, J. A dendrite method for cluster analysis. *Communications in Statistics - Theory and Methods* **3**, 1–27 (1974).

73. Rousseeuw, P. J. Silhouettes: A graphical aid to the interpretation and validation of cluster analysis. *Journal of Computational and Applied Mathematics* **20**, 53–65 (1987).

74. Davies, D. L. & Bouldin, D. W. A cluster separation measure. *IEEE Trans. Pattern Anal. Mach. Intell.* **1**, 224–227 (1979).

75. Wang, J., Wen, S., Symmans, W. F., Pusztai, L. & Coombes, K. R. The bimodality index: a criterion for discovering and ranking bimodal signatures from cancer gene expression profiling data. *Cancer Inform.* **7**, 199–216 (2009).

76. Hartigan, J. A. & Hartigan, P. M. The Dip Test of Unimodality. *Ann. Statist.* **13**, 70–84 (1985).

77. Simpson, E. H. Measurement of Diversity. *Nature* **163**, 688–688 (1949).

78. Hsu, L. L. & Culhane, A. C. Correspondence analysis for dimension reduction, batch integration, and visualization of single-cell RNA-seq data. *Sci. Rep.* **13**, 1197 (2023).

79. Shannon, C. E. A mathematical theory of communication. *Bell System Technical Journal* **27**, 379–423 (1948).

80. Reimand, J., Kull, M., Peterson, H., Hansen, J. & Vilo, J. g:Profiler--a web-based toolset for

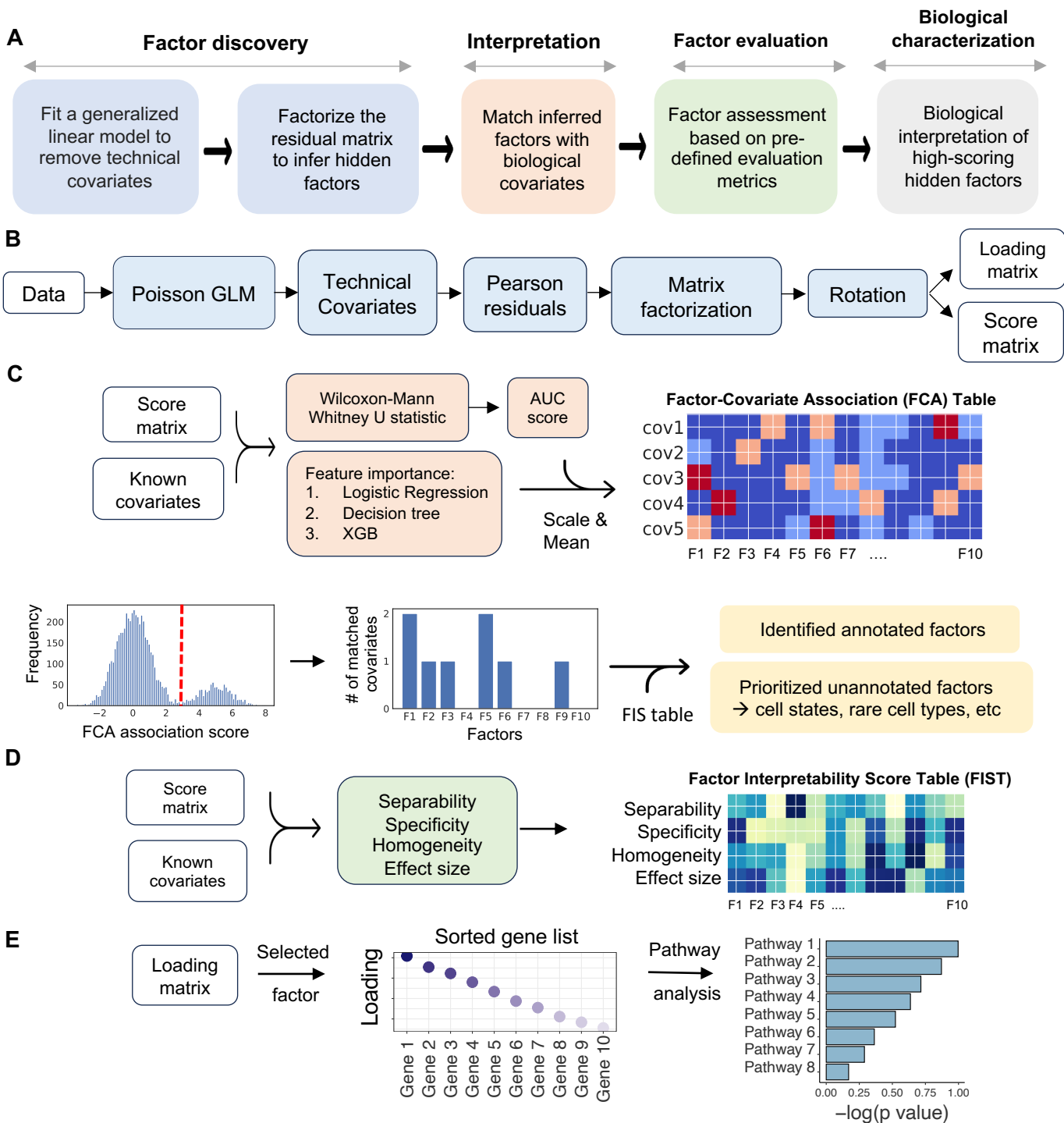functional profiling of gene lists from large-scale experiments. *Nucleic Acids Res.* **35**, W193-200 (2007).
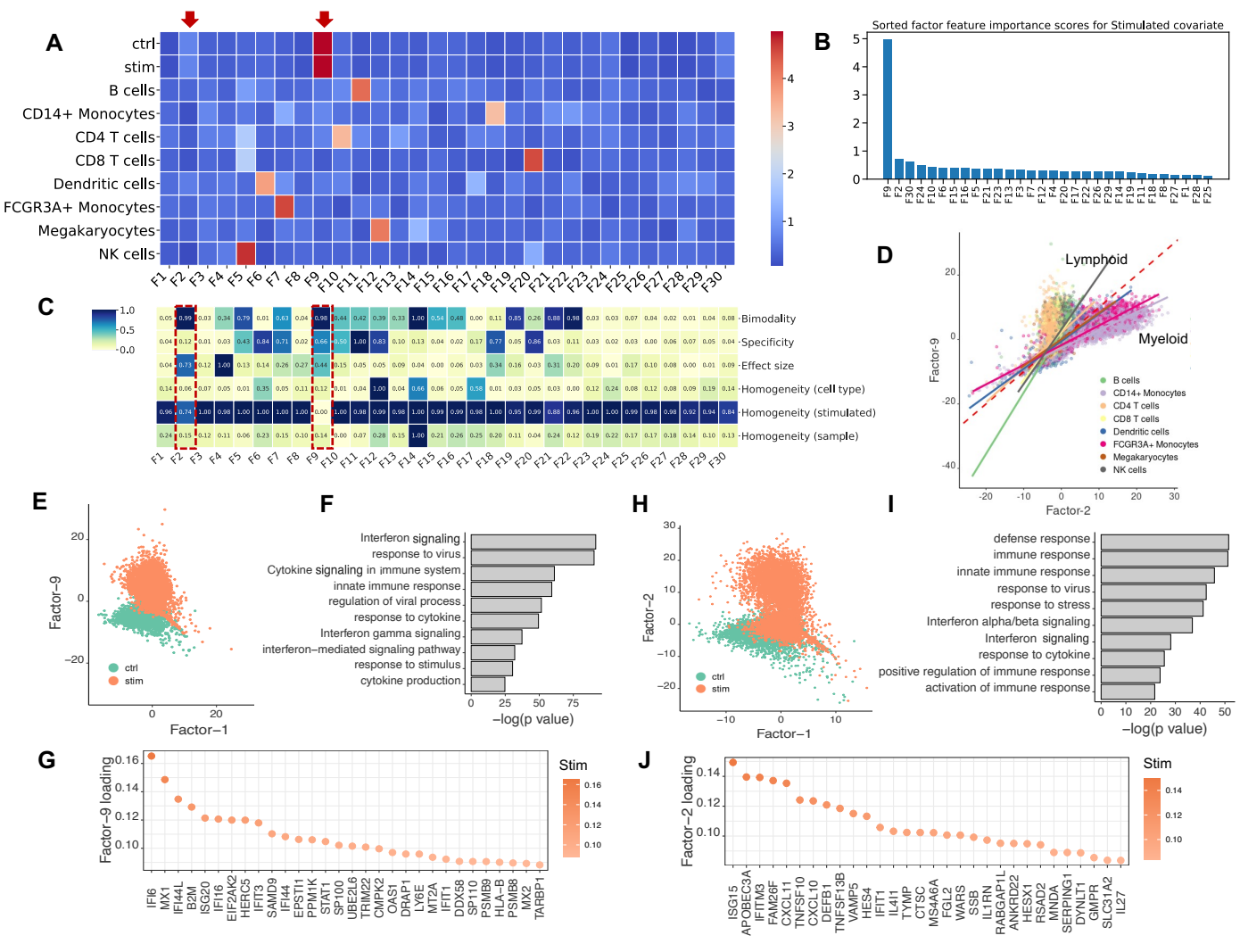
Figure 1) sciRED overview.

Figure 2) Deciphering cell type identity programs and sex-specific processes in a human healthy kidney map.

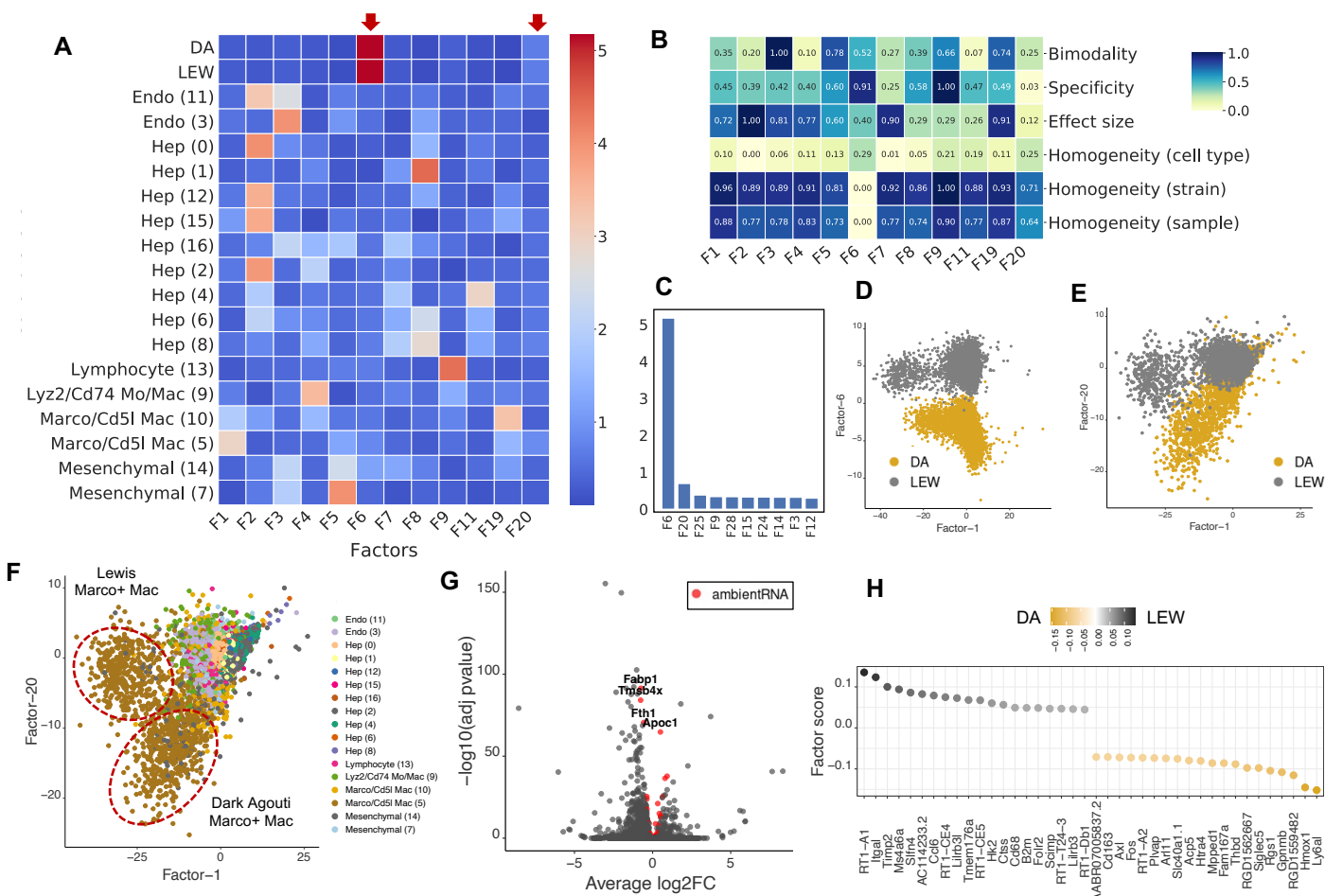Figure 3) Identifying interferon-β stimulation signals across lymphoid and myeloid cells in a PBMC dataset.

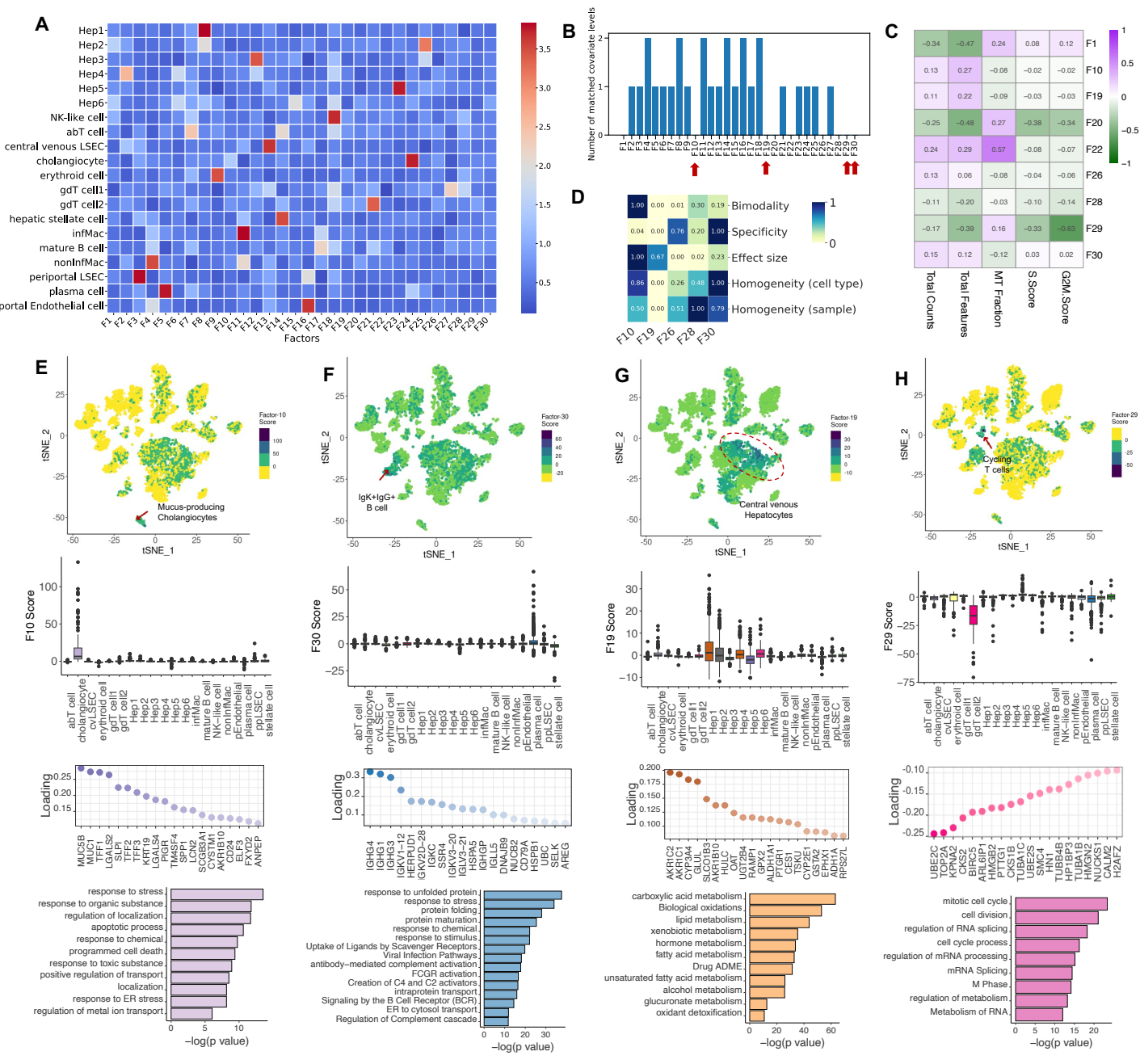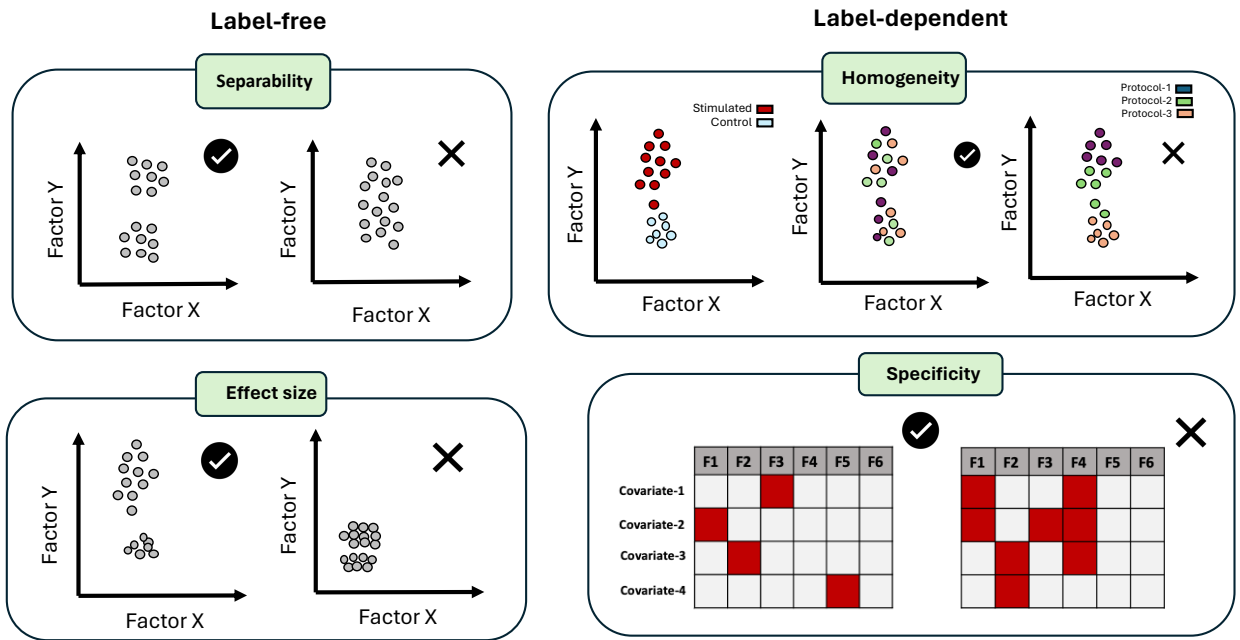Figure 4) sciRED identifies strain-based variation despite ambient RNA contamination in a rat liver map.

Figure 5) Exploring hidden biology in the healthy human liver atlas using unannotated factors.

Supplementary Figure 1) Schematic overview of factor interpretability metrics
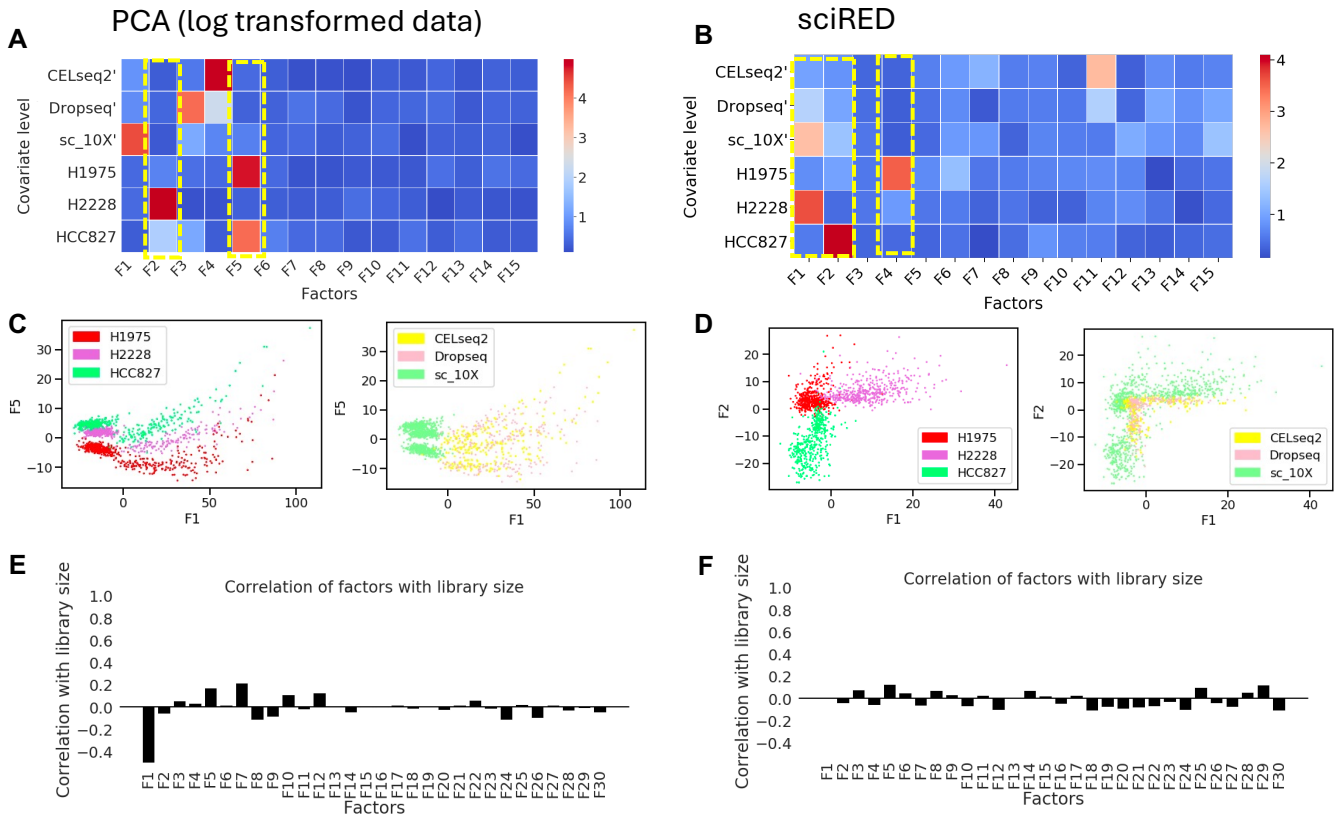
Supplementary Figure 2) Enhanced interpretability of factors achieved by removing technical confounders.
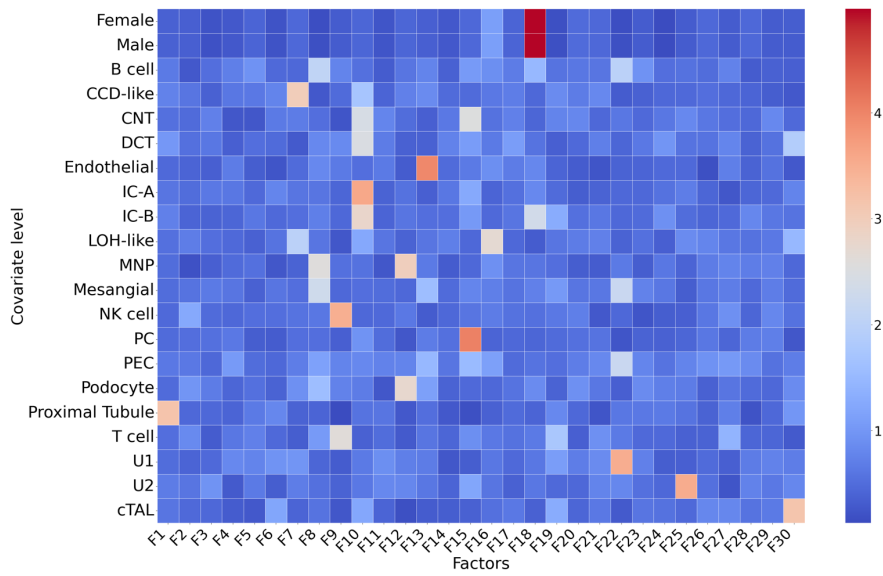
Supplementary Figure 3) The complete factor-covariate association table of the healthy kidney atlas.
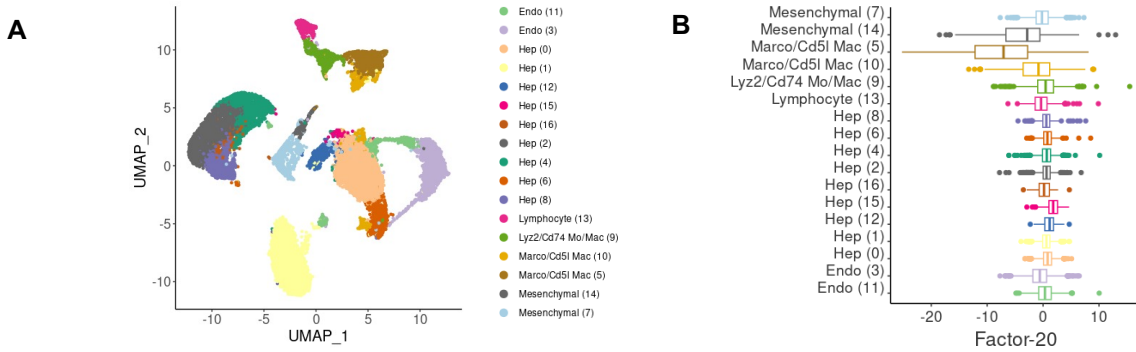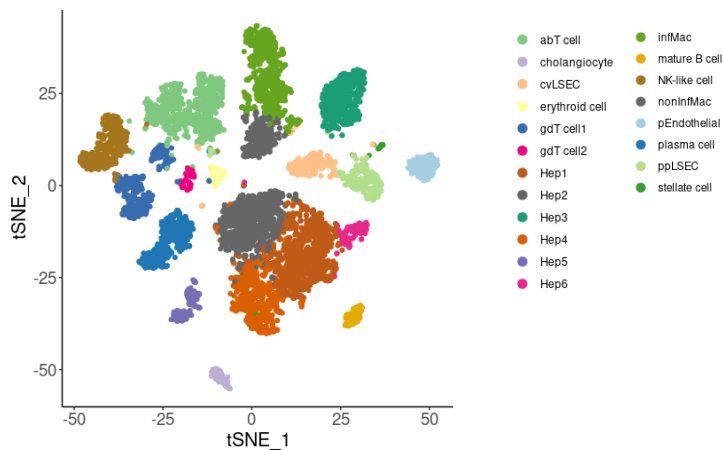
Supplementary Figure 4) Annotated healthy rat liver map

Supplementary Figure 5) Annotated healthy human liver map
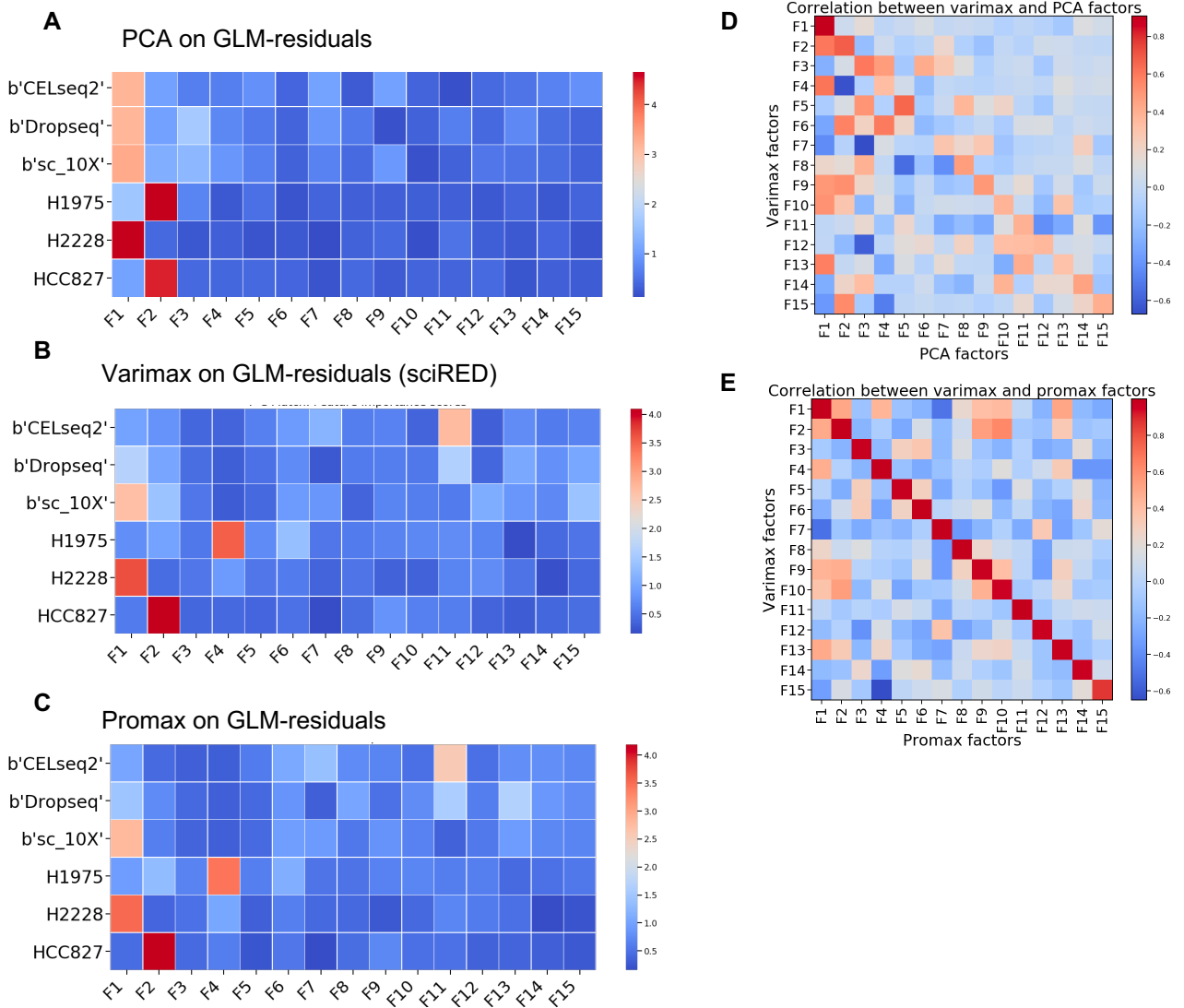
A PCA on GLM-residuals

B Varimax on GLM-residuals (sciRED)

C Promax on GLM-residuals

D Correlation between varimax and PCA factors

E Correlation between varimax and promax factors

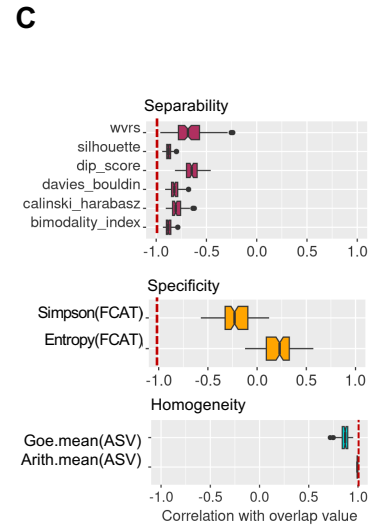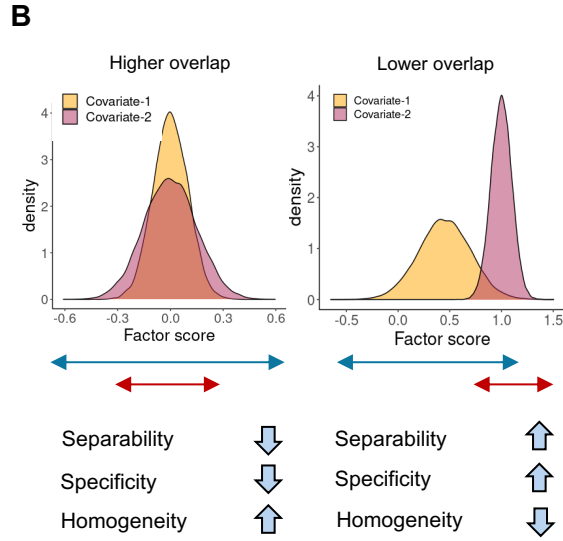Supplementary Figure 6) Enhancement in identifying cell line-specific factors through rotations.
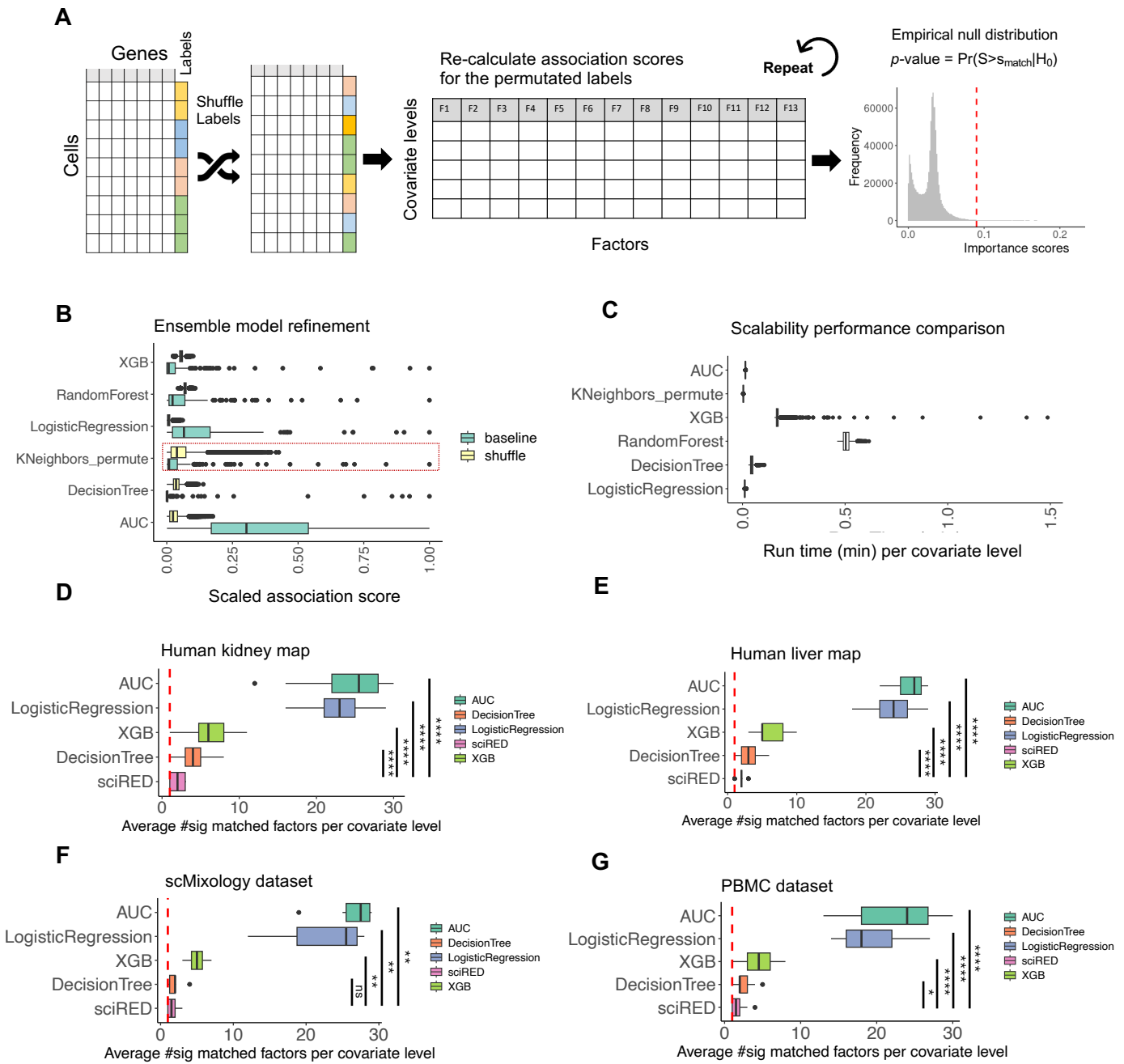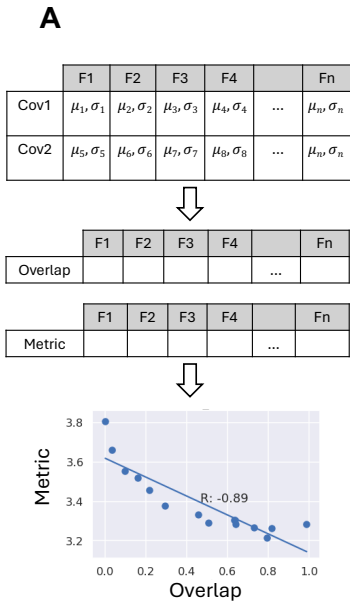
Supplementary Figure 7) Performance evaluation and benchmarking of sciRED.
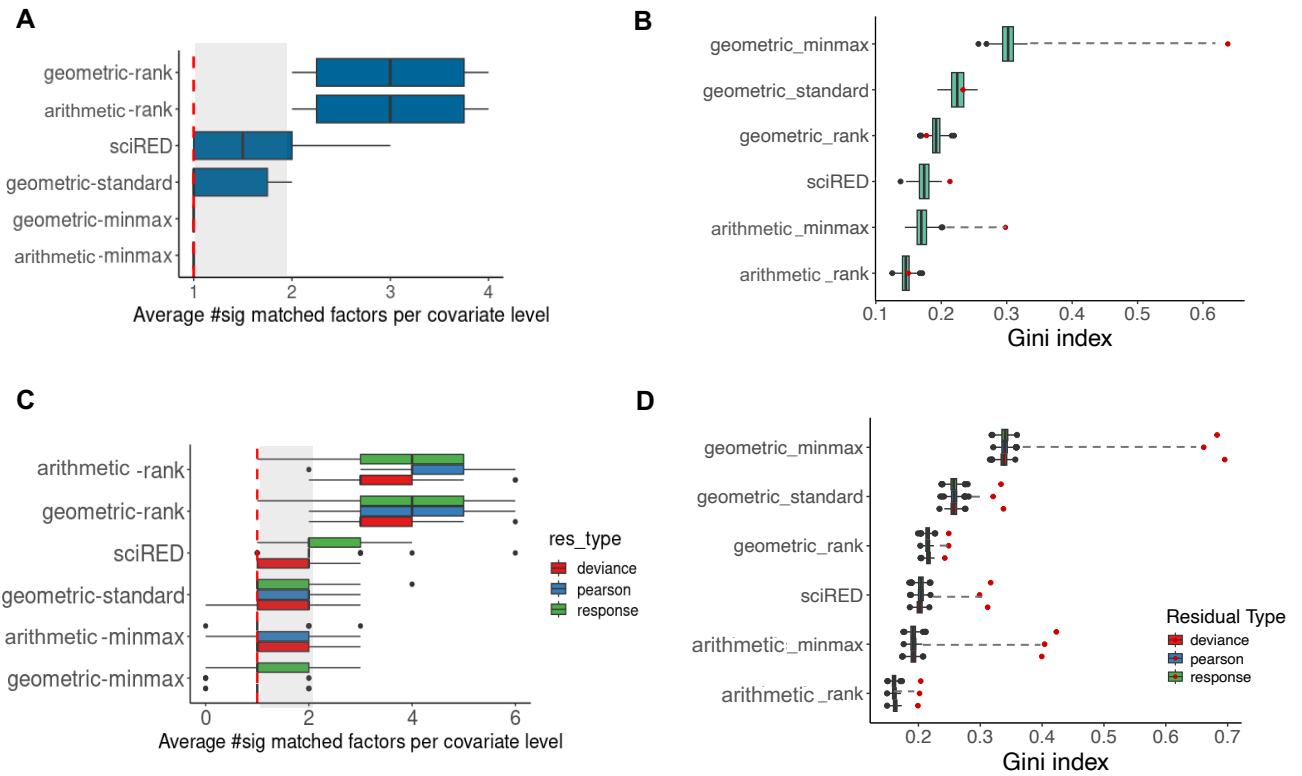
Supplementary Figure 8) Optimizing ensemble design through permutation-based comparison of scaling and mean calculation methods.
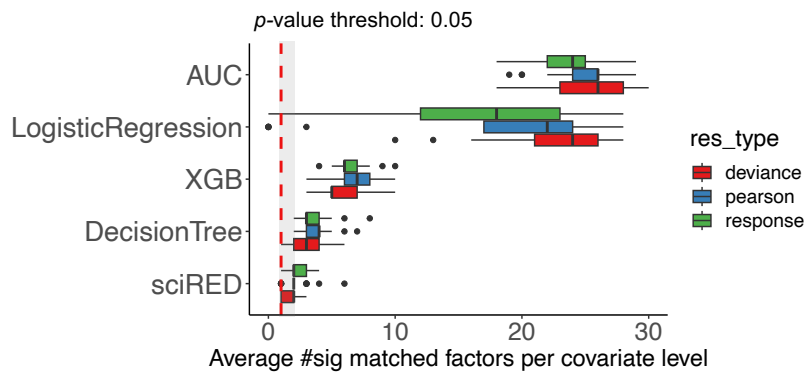
Supplementary Figure 9) Impact of residual choice on factor interpretability.

Supplementary Figure 10) Evaluating factor interpretability metrics through factor simulation